Article

Not peer-reviewed version

ML-Driven In Vitro Remodeling of Alveolar Macrophage Profiles from Bronchoalveolar Lavage Fluid: A Novel Approach for Personalized Therapy in Severe Respiratory Diseases

Igor D. Zlotnikov , Alexander A. Vinogradov , Elena V. Kudryashova *

Posted Date: 17 March 2026

doi: 10.20944/preprints202603.1206.v1

Keywords: macrophage polarization; bronchoalveolar lavage fluid (BALF); personalized medicine; M1/M2 macrophages; antibiotics; cytostatic drug; in vitro remodeling; ML; Linear discriminant analysis

 doi:10.20944/preprints202603.1206.v1

Article

ML-Driven In Vitro Remodeling of Alveolar Macrophage Profiles from Bronchoalveolar Lavage Fluid: A Novel Approach for Personalized Therapy in Severe Respiratory Diseases

Igor D. Zlotnikov [1], Alexander A. Vinogradov [2] and Elena V. Kudryashova [1]*

[1] Central University, 7 Gasheka St., Moscow 123056, Russia
[2] Centre for Mathematical Plasma-Astrophysics, KU Leuven, Leuven, Belgium
* Correspondence: helenakoudriachova@yandex.ru

Abstract

The secondary immunomodulatory effects of conventional therapeutics, such as antibiotics and cytostatics, are frequently overlooked despite their significant clinical implications. Building on our previous findings that drugs like paclitaxel and doxorubicin heavily influence macrophage polarization—potentially driving metastasis or inflammation—this study systematically evaluates the secondary immune-modulating actions of standard drugs and natural adjuvants. Using patient-derived bronchoalveolar lavage (BAL) fluid (ex vivo alveolar macrophages), we developed an analytical platform using synthetic carbohydrate-functionalized fluorescent ligands targeting key receptors (CD206, CD209, CD280, CD301). Integrating ligand-binding profiles with Linear Discriminant Analysis (LDA) yielded quantitative immune-state vectors capable of differentiating between favorable prognostic signatures and imbalanced immune states. Profiling samples across heterogeneous respiratory conditions revealed highly context-dependent responses. While some treatments synergistically corrected imbalanced profiles, others provoked dysregulation. Notably, in pneumonia or bronchitis with an asthma-prone M2-dominant profile, specific antibiotic regimens are critical; doxycycline, for instance, may exacerbate patient deterioration by further driving M2a polarization. Crucially, we identified that natural adjuvants (e.g., curcumin, coumarins, polyphenols) exhibit potent properties capable of correcting these adverse secondary drug effects. Ultimately, this profiling platform highlights the necessity of evaluating patient-specific secondary drug effects, offering a functional blueprint for precision immunotherapy and the rational design of adjuvant-enhanced treatments.

Keywords: macrophage polarization; bronchoalveolar lavage fluid (BALF); personalized medicine; M1/M2 macrophages; antibiotics; cytostatic drug; in vitro remodeling; ML; Linear discriminant analysis

1. Introduction

Macrophages are highly dynamic and functionally heterogeneous populations of innate immune cells that play multifaceted roles in tissue homeostasis, immune surveillance, and host defense [1]. These cells are distributed throughout virtually all tissues, where they function as central regulators of the immune response [2]. A defining characteristic of macrophages is their exceptional functional plasticity—their capacity to rapidly adapt phenotype and function in response to diverse microenvironmental signals, including microbial products, damaged cells, and specific cytokines [3–

 doi:10.20944/preprints202603.1206.v1

7]. This adaptability positions macrophages as key players in both the successful resolution of inflammation and the development of chronic pathologies.

The classical M1/M2 polarization paradigm provides a fundamental framework for understanding macrophage function, categorizing them into two functionally distinct subsets [8–13]. M1, or classically activated, macrophages are induced by pro-inflammatory signals such as interferon-gamma (IFN-γ) and lipopolysaccharide (LPS). They are characterized by production of pro-inflammatory cytokines (TNF-α, IL-6, IL-12), possess potent microbicidal and cytotoxic properties, and are crucial for mounting Th1-type immune responses against intracellular pathogens and tumors [14–16]. In contrast, M2, or alternatively activated, macrophages are induced by anti-inflammatory cytokines (IL-4, IL-13) and are involved in immunoregulation, wound healing, tissue remodeling, and angiogenesis, primarily through secretion of anti-inflammatory agents such as IL-10 [17–21].

However, the binary M1/M2 model is now recognized as an oversimplification. In vivo, macrophage phenotypes exist not as discrete states but as a dynamic continuum, with intermediate and hybrid profiles shaped by the complex local tissue environment [22–24]. For instance, recent comparative studies (Sun et al., 2026) revealed that distinct tissue niches drive divergent immune responses: unlike liver injuries dominated by lymphocytes, cardiac trauma recruits specific CCRL2+ macrophages that co-express pro-inflammatory cytokines yet primarily drive fibrosis through direct fibroblast modulation [25]. Crucially, dysregulation of macrophage polarization axis is a defining feature of numerous pathologies, where the dominant macrophage profile often dictates disease progression and clinical outcome [26].

In oncology, prevalence of M2-like tumor-associated macrophages (TAMs) is well-documented as a factor for poor prognosis, promoting tumor growth, angiogenesis, metastasis, and multidrug resistance [8,27–30]. In tuberculosis infection, M1 macrophage activation is essential for controlling *Mycobacterium tuberculosis* [31,32], while insufficient M1 activity fails to eliminate the pathogen, leading to chronic infection [33,34]. Similarly, in pulmonary diseases such as idiopathic pulmonary fibrosis (IPF) and chronic obstructive pulmonary disease (COPD), persistent aberrant macrophage activation within the bronchoalveolar lavage fluid is associated with disease severity and unresolved inflammation [35,36]. Although recent comprehensive and methodologically complex efforts have highlighted that clinical trajectories are dictated by specific functional macrophage 'fingerprints' rather than a binary M1/M2 ratio [37], these massive studies have thus far provided limited practical understanding or translational value.

Recent evidence, including our own work on doxorubicin-induced macrophage modulation [38], has revealed that the immunomodulatory impact of drugs constitutes a critical "hidden layer" of pharmacology [39]. While primarily designed to target malignancies or pathogens, many pharmacological agents—such as cytostatics and antibiotics—exhibit secondary activities that inadvertently remodel the immune landscape. These off-target effects can profoundly influence macrophage polarization, creating a therapeutic paradox. For example, despite its potent cytostatic efficacy, we recently demonstrated that doxorubicin can paradoxically induce an immunosuppressive M2-like macrophage phenotype [38]. This shift fosters a pro-tumorigenic environment associated with the emergence of tumor-associated macrophages (TAMs), promoting metastatic dissemination and contributing to multidrug resistance [40].

Conversely, other agents can restore antitumor immunity. Paclitaxel, a classical microtubule-stabilizing chemotherapeutic, promotes a pro-inflammatory M1 phenotype by activating Toll-like receptor 4 (TLR4) signaling and amplifying NF-κB–mediated transcriptional programs [41,42], effectively converting immunologically "cold" (M2-rich) tumors into "hot" immune-active niches.

Importantly, the context-dependent nature of these phenotypic transitions underscores that macrophage plasticity is not merely a side effect of therapy, but a primary therapeutic target that can be harnessed to optimize treatment outcomes. To map these complex dynamics, it is crucial to consider a diverse array of pharmacological agents spanning multiple therapeutic classes, including

 doi:10.20944/preprints202603.1206.v1

antibiotics, cytostatics, and adjuvants such as terpenoid-based efflux pump inhibitors, metabolic regulators, and microenvironment modifiers.

Among these, curcumin—a bioactive compound renowned for its potent anti-inflammatory activity via NF-κB inhibition—also acts as an effective TAM reprogrammer in cancer contexts [43,44]. Given its previously demonstrated direct synergistic cytotoxicity when combined with doxorubicin against cancer cells [45,46], curcumin emerges as an ideal adjuvant candidate. Similarly, coumarins and their derivatives, such as 4-methylumbelliferone (MUmb), exhibit intricate, context-dependent immunomodulatory properties [47,48], positioning them as promising adjuvants for chemotherapy.

The landscape of potential immunomodulators extends further to agents with highly nuanced immune profiles. For instance, the broad-spectrum antibiotic doxycycline, while classically defined as an anti-inflammatory agent, exerts secondary effects as an inhibitor of matrix metalloproteinases, and emerging evidence indicates it may also actively inhibit M2 polarization [49,50]. Other notable modulators include the antioxidant glutathione [10], which influences polarization via oxidative stress pathways, and the antidiabetic agent metformin, known to attenuate M2 polarization through the activation of the AMPK (AMP activated protein kinase) pathway. Beyond these established therapeutics, novel synthetic compounds—specifically chromene derivatives [51] and chalcone analogs [52]— offer profound potential to actively drive macrophage repolarization.

The ex vivo platform presented in this study offers a robust and highly relevant system for screening novel synthetic drugs, nutraceuticals, and immunoadjuvants. Ultimately, rational drug design must integrate these complex immunomodulatory dynamics to accurately predict net clinical outcomes. By facilitating the comprehensive assessment of macrophage repolarization prior to costly clinical trials, our methodology empowers precisely this predictive approach. To achieve this level of clinical relevance, the platform utilizes bronchoalveolar lavage (BAL)—a standard clinical procedure that provides a unique window into the lung's immune landscape. Because BAL yields a rich, patient-derived cellular population comprising up to 85% disease-relevant alveolar macrophages, it serves as the ideal physiological model for translating these ex vivo screenings into personalized therapeutic strategies [36,53–61]. We have recently developed a novel methodology for high-dimensional profiling of macrophage subpopulations based on a unique panel of carbohydrate ligand markers targeting C-type lectin receptors (CD206, CD209, CD280, CD301) [37], ligand markers targeting CD68 [39], combined with assessment of phagocytic capacity [62]. By applying this technique to BAL-derived macrophages, we can establish distinct functional "fingerprints" that correlate with either favorable disease resolution or poor prognosis characterized by M1/M2 imbalance.

Current approaches to macrophage phenotyping rely heavily on systemic cytokine analysis. However, these methods are largely restricted to fundamental research; despite their methodological complexity, they often yield negligible clinical utility and lack direct translational value [25]. To bridge this gap, we hypothesize that a standardized ex vivo platform applied to patient-derived alveolar macrophages constitutes a pivotal tool for personalized medicine. This approach enables the rational selection of therapies tailored to the patient's specific immune endotype. In this study, we establish a robust model to define prognostic polarization signatures associated with distinct clinical trajectories. By benchmarking reference pro- and anti-inflammatory agents against novel formulations, we aim to uncover latent macrophage reprogramming, thereby distinguishing therapeutic efficacy from unintended immunotoxicity. Crucially, this analytical framework facilitates the systematic evaluation of immunoadjuvants, allowing for the precise selection of optimal drug formulations. To process the complex, high-dimensional datasets generated by such evaluations, artificial intelligence approaches—including random forests and artificial neural networks—offer immense predictive potential. In the present study, however, we relied exclusively on Linear Discriminant Analysis (LDA) to robustly classify and model these macrophage polarization states. Consequently, this work proposes a standardized technology for the preclinical assessment of drug-induced immune remodeling, uniquely designed to predict adverse long-term effects prior to clinical application.

 doi:10.20944/preprints202603.1206.v1

2. Results and Discussion

2.1. Potential for Therapeutic Macrophage Reprogramming in Airway Diseases

Macrophages are pivotal orchestrators of inflammatory diseases, wielding significant control through secretion of pro-inflammatory mediators and counter-regulatory factors that drive or resolve inflammation. The remarkable plasticity of macrophages allows them to adopt diverse functional phenotypes, ranging from resting M0 state through pro-inflammatory M1 state to multiple anti-inflammatory and pro-resolution M2 subsets (M2a, M2b, M2c, M2d) [63]. Recognizing this inherent heterogeneity, we developed a comprehensive macrophage polarization profiling strategy for individual patients with distinct respiratory conditions: bronchitis (acute inflammation), bronchial asthma (allergic/eosinophilic), and bronchiectasis (chronic remodeling).

Figure 1 outlines the complete workflow for isolating, treating, and phenotypically characterizing alveolar macrophages from BALF to assess therapeutic reprogramming potential. The workflow begins with isolation of alveolar macrophages from patient BALF, followed by enrichment through adherence to mannan-coated surfaces to selectively culture macrophages while excluding other immune cell types. Following isolation, macrophages are allocated to distinct experimental groups: (i) M0 baseline (no additives), (ii) M1 polarization control (LPS + IFNγ), (iii) M2a polarization control (IL-4), and experimental groups treated with pharmacological agents. Following a 24-hour period of incubation, macrophages are subjected to phenotypic profiling using a panel comprising five FITC-labelled carbohydrate ligands, designated L1 through L5, each bearing mannose, galactose, or trimannose fragments that target specific receptors such as CD206, CD209, CD280, and CD301. This multiparametric approach enables precise discrimination of M0, M1, and M2a phenotypes based on unique receptor expression patterns, quantified through fluorescence intensity and ligand binding analysis.

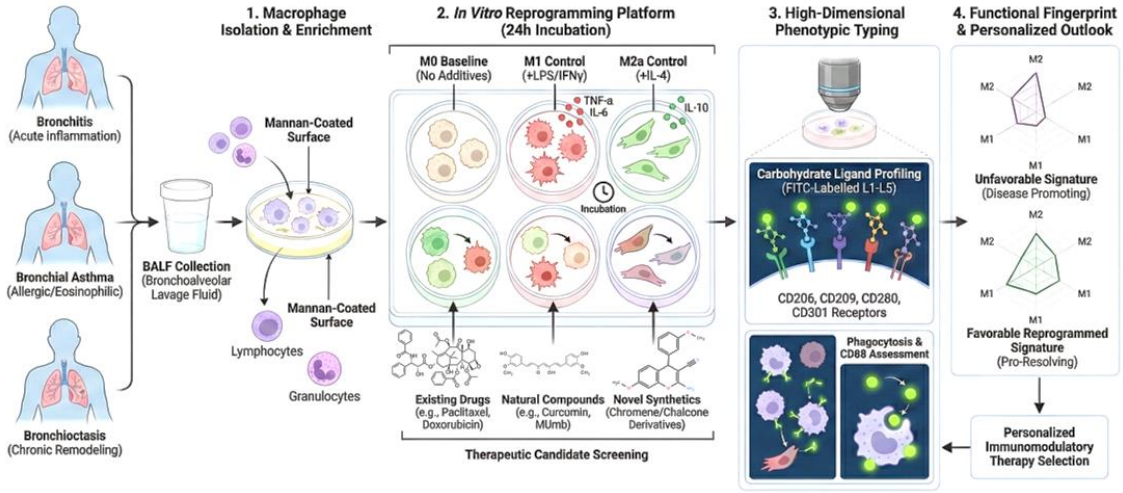

Figure 1. Experimental scheme for macrophage reprogramming and phenotypic typing. The platform was validated using BALF samples from patients with distinct respiratory conditions, specifically: bronchitis (acute inflammation), bronchial asthma (allergic/eosinophilic), and bronchiectasis (chronic remodeling).

The resultant polarization profiles allow objective tracking of therapeutic remodeling and identification of compounds that effectively shift macrophage populations between M1 and M2 states, or toward balanced M0/M1/M2 ratios conducive to disease resolution. Expected outcomes include discovery of novel therapeutic agents and deeper mechanistic understanding of their actions at the carbohydrate receptor level, paving the way for personalized immunomodulatory strategies to combat severe respiratory diseases.

 doi:10.20944/preprints202603.1206.v1

2.2. Development and Characterization of Carbohydrate-Functionalized Fluorescent Ligands for Multiparametric Macrophage Typing

2.2.1. Physicochemical Parameters and Design Rationale

In order to conduct a comprehensive analysis of alveolar macrophages using multiple parameters, we implemented a series of fluorescent ligands based on carbohydrates (Figure S1). Based on our previous research [64], which involved the synthesis and validation of FITC-labelled polymers conjugated with specific carbohydrate units, we have now demonstrated their capacity for selective binding to various macrophage surface receptors. This allows for precise phenotypic differentiation. Table 1 summarizes the designation, physicochemical parameters, and specificity of five carbohydrate-functionalized fluorescent ligands for macrophage receptors. The ligands were designed based on systematic variation of carbohydrate type (mannose vs. galactose), configuration (linear vs. cyclic), and degree of functionalization to optimize receptor binding specificity and efficiency for discriminating M0, M1, M2a, M2b, M2c, and M2d macrophage subpopulations.

Table 1. Designation, physicochemical parameters and specificity of carbohydrate-functionalized fluorescent ligands for macrophage receptors. PBS (0.01 M, pH 7.4). T = 37 °C.

Ligand	Designation	Molar ratio	Hydrodynamic diameter, nm *	ζ-potential, mV *	Binding with CD206+ macrophage, % **	Predicted affinities for macrophage receptors, pK_{dis}***			
						CD206 (Mannose receptor)	CD209 (DC-SIGN)	CD280 (MRC2/ Endo180)	CD301 (MGL)
L1	Man_{Lin}-PEI-FITC	15:1:1	105 ± 10	+10 ± 2	38 ± 3	5.2	5.0	4.1	4.0
L2	Man_{Cyc}-PEI-FITC	18:1:1	115 ± 15		60 ± 7	6.5	5.8	4.5	4.1
L3	Gal_{Lin}-PEI-FITC	16:1:1	110 ± 15		14 ± 2	4.0	4.1	4.3	5.2
L4	Gal_{Cyc}-PEI-FITC	13:1:1	115 ± 10		48 ± 4	5.1	5.3	4.0	6.8
L5	triMan-$GlcNAc_2$-PEI-FITC	10:1:1	130 ± 20		80 ± 6	7.4	6.7	6.1	4.9

*measured by DLS; ** by flow cytometry; *** affinities represent in silico neural-network–based binding predictions using Pafnucy neural network [65,66].

Figure S1 provides a schematic overview of the synthetic approach employed to generate these FITC-labeled fluorescent probes, incorporating five distinct carbohydrates with receptor-specific recognition properties. Successful synthesis of the fluorescently labeled polymeric conjugates is corroborated by spectroscopic analyses. FTIR spectra (Figure S2) clearly show characteristic vibrational modes of PEI backbone (CH_2 stretching at 2980-2800 cm^{-1}) and FITC label (C=C at 1580 cm^{-1} and 1450 cm^{-1}), along with C–N and C–O–C bonds indicative of PEI-saccharide conjugation (1200-1000 cm^{-1}). ^1H NMR data further confirms the successful assembly (Figure S3), displaying expected proton signals for the appended carbohydrate moieties (e.g., mannose signals at 3.9–5.3 ppm) alongside characteristic PEI polymer resonances (around 2.5–2.9 ppm). The absence of anomeric proton signals in some Gal-PEI and Man-PEI conjugates, along with slight shifts in carbohydrate proton signals, suggests successful modification and conjugation at the reducing end of the sugar residues.

Ligands panel builds upon our prior synthesis of FITC-labeled polymers conjugated to distinct carbohydrate moieties, now refined to selectively bind to diverse macrophage surface receptors and

 doi:10.20944/preprints202603.1206.v1

facilitate precise phenotypic discrimination. The designation, molar ratio of components (carbohydrate:PEI:FITC), hydrodynamic diameter, zeta potential, percentage of CD206+ macrophages, and predicted receptor affinity for each ligand are summarized in the Table 1.

To mechanistically validate receptor specificity and precisely delineate the cellular polarization status, we employed competitive inhibition assays utilizing mannan. As a polymannose polysaccharide, mannan acts as a specific competitive inhibitor for the carbohydrate recognition domains of CD206 and CD209, allowing us to establish distinct functional profiles for each macrophage subpopulation. Crucially, the identification of classically activated M1 macrophages inherently relies on the absence of mannan inhibition. Because the M1 phenotype lacks significant expression of mannose-specific receptors, the binding of fluorescent ligands persists unabated even in the presence of the inhibitor. Conversely, the M2a phenotype, representing the prototypical alternatively activated state, exhibits robust expression across the entire targeted receptor panel—including CD206, CD209, CD280, and CD301. Consequently, M2a cells display maximal initial multivalent ligand binding, which is subsequently and profoundly abrogated following mannan competition. The regulatory M2b subtype, in contrast, is characterized by a weak, residual expression of CD206 and a complete absence of CD209 and CD301, resulting in an overall low binding profile with minimal susceptibility to mannan blockade. Furthermore, M2c macrophages, typically associated with tissue remodeling, present high CD206 and moderate CD280 levels but lack CD209 and CD301; thus, they exhibit strong mannan-inhibited binding of mannose-based ligands while remaining unresponsive to galactose-targeted probes, distinctly separating them from the M2a cluster. Finally, unpolarized M0 macrophages maintain a low expression of mannose receptors without definitive activation markers.

2.2.2. Flow Cytometry Analysis of Ligand Binding Specificity to Macrophages vs. BALF Cells

Prior to evaluating the specific receptor-targeting efficacy of the synthesized polymer-ligand conjugates, flow cytometry was employed to rigorously ascertain both the overall cellularity and the extent of cell viability across the standardized macrophage populations (M0, M1, and M2a). Once optimal culture health and baseline phenotypic integrity were confirmed, we established the fundamental binding profiles of the fluorescent probes within this controlled in vitro setting (Figure S4, Supplementary Materials). As illustrated in Figure S4, the engineered ligands exhibited distinct, structure-dependent binding affinities, thereby providing a crucial functional baseline for validating receptor specificity prior to deploying the platform on complex, patient-derived ex vivo samples. The branched trimannose (L5, triMan-GlcNAc$_2$-PEI-FITC) and cyclic mannose (L2, Man$_{Cyc}$-PEI-FITC) displayed pronounced rightward shifts in histograms with mean fluorescence intensity (MFI) values 3–4-fold higher than the control. Specifically, the cyclic derivative L2 demonstrated significantly higher binding efficiency (~60%) compared to the linear analogue L1 (Man$_{Lin}$-PEI-FITC, ~38%), suggesting that the cyclic conformation provides an optimized geometry for C-type lectin receptors such as CD206. A similar trend was observed for galactose-targeting ligands, where the cyclic scaffold L4 (Gal$_{Cyc}$-PEI-FITC) significantly outperformed its linear counterpart L3 (GalLin-PEI-FITC) (~48% vs. ~14%), confirming the structural advantage of cyclic systems for lectin recognition in a purified cellular model.

To validate receptor targeting in a physiological context, we introduced the synthesized conjugates to primary alveolar macrophages isolated from patient BALF fluid. Unlike the uniform binding profiles observed in THP-1-derived macrophages—which serve as a standardized model for defined polarization states—the analysis of these clinical samples revealed a far more complex landscape (Figure 2), significantly influenced by patient-specific heterogeneity.

Within the patient-derived BALF samples, flow cytometry analysis confirmed both the specific binding profiles of our synthesized ligands and the preservation of overall macrophage cellularity and viability. As anticipated, the linear galactose ligand L3 acted as a reliable negative control, exhibiting negligible cellular interaction (0.61% positive cells, Figure 2b). In contrast, mannosylated

 doi:10.20944/preprints202603.1206.v1

ligands demonstrated differential, receptor-specific uptake: the linear mannose L1 achieved moderate capture (11.51% positive cells, Figure 2c), consistent with monomeric mannose's known affinity for the CD206 receptor. The cyclic mannose derivative L2 yielded a slightly higher positive population (15.18%, Figure 2d); while this aligns with the higher affinity trend observed in standardized cell lines (Figure S4), the less pronounced difference in the ex vivo BALF samples is likely attributable to inherent macrophage heterogeneity. Crucially, accurate profiling requires that the polymeric backbone does not compromise the sample. Flow cytometry viability assays demonstrated that while unmodified PEI induces extensive cytotoxicity within 3 hours (only 42% viable cells remaining), all saccharide-modified PEI conjugates—including PEI-mannose, PEI-trimannose, and PEI-galactose—are fully biocompatible. These modifications ensure that high cell viability (>88%) and the overall cellularity of the target macrophage populations are robustly maintained throughout the assay.

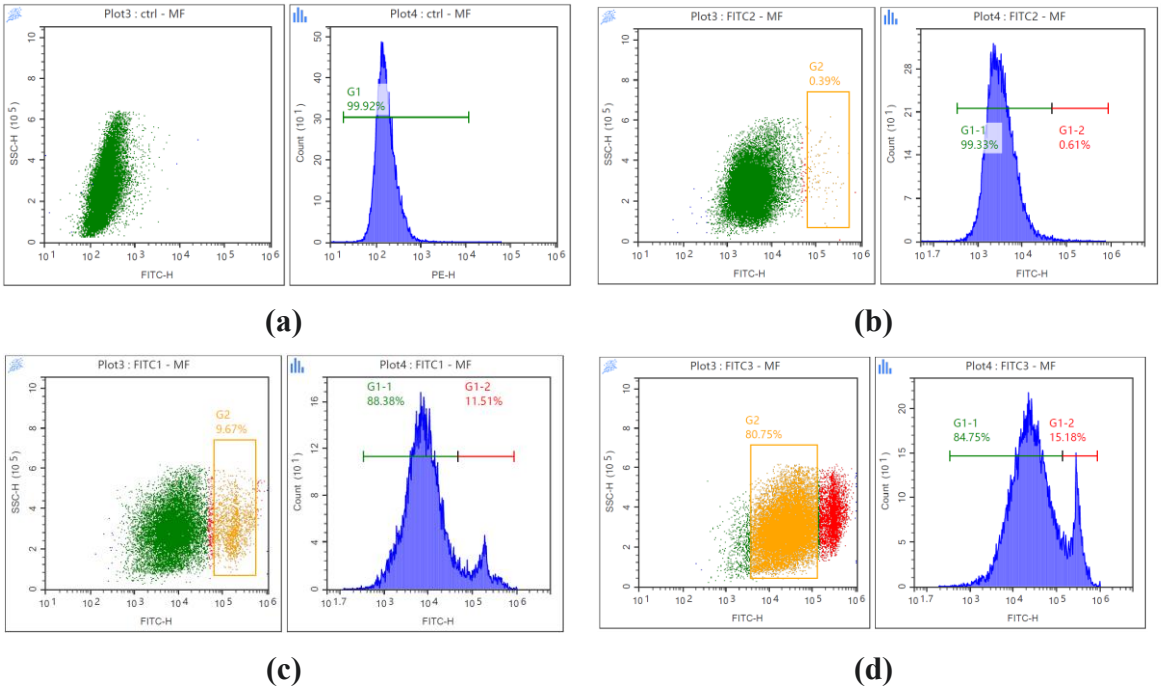

Figure 2. Flow cytometric analysis of ligand binding profiles in BALF macrophages. Representative dot plots (Left: SSC-H vs. FITC-H) and corresponding fluorescence intensity histograms (Right: Count vs. FITC-H) are shown for each condition. The gates indicate the population of cells exhibiting positive ligand binding (G1-2) versus the negative population (G1-1). (a) Intact BAL cells (control). (b) Cells incubated with linear FITC-PEI-galactose. (c) Cells incubated with linear FITC-PEI-mannose. (d) Cells incubated with cyclic FITC-PEI-mannose.

In conclusion, the flow cytometry analysis demonstrates the successful registration of ligand interactions with macrophage surface receptors directly within heterogeneous BALF samples. The result established that the trimannose ligand possesses the highest overall affinity, however the key finding is that the tested ligands exhibit distinct, yet comparable, binding affinities to macrophages. With pK_{dis} ranging broadly from 3 to 7, this varied affinity profile is highly advantageous. It allows the probes to generate unique binding "fingerprints," making it possible to detect subtle differences in receptor expression levels, surface clustering, and the structural microheterogeneity of macrophage populations. Building on this capacity for sensitive and selective profiling, we extended the study to evaluate their diagnostic applicability. The following section details the application of these probes in characterizing macrophage populations within clinical patient samples.

 doi:10.20944/preprints202603.1206.v1

2.3. Patient Cohort and Peripheral Blood and Bronchoalveolar Lavage Analysis

The study cohort comprised ten pediatric patients (age range 6–16 years; median 10.5 years) admitted with respiratory pathologies. Diagnoses included bronchiectasis (n=4), bronchial asthma (n=5), and acute bronchitis (n=1). Routine hematological assessment involved a Complete Blood Count (CBC) with a full leukocyte differential (evaluating neutrophils, lymphocytes, monocytes, eosinophils, and basophils) alongside serum C-reactive protein (CRP) quantification to establish baseline systemic inflammatory profiles (Table 2).

These parameters were integrated to calculate a clinical disease severity score, ranging from 0 (favorable prognosis) to 5 (poor prognosis). The cohort demonstrated significant heterogeneity in inflammatory responses. Patients with a Severity Score of 0 (P6, P8) exhibited physiological values across all parameters and a favorable prognosis. The majority of the cohort (n=6) clustered into an intermediate severity group (Scores 1–2), characterized by a neutral prognosis. Within this cluster, specific inflammatory deviations were observed, including elevated CRP levels in P2, P4, and P10 (range 6.5–12.0 mg/L) and prominent leukocytosis in P3. High disease severity (Scores 3 and 5) was identified in two patients: P5, presenting with acute bronchitis and fever (38 °C) alongside marked CRP elevation (44.7 mg/L); and P1, presenting with bronchiectasis, severe leukopenia (WBC 2.16 × 10^9/L), and monocytosis.

Table 2. Complete blood count (CBC) parameters and peripheral inflammatory markers in pediatric patients with respiratory disease. The de-identified cohort (P1–P10) includes age, sex, diagnosis, fever status, total white blood cell (WBC) count, leukocyte differential (neutrophils, eosinophils, and monocytes; %), serum C-reactive protein (CRP), and a clinical disease severity score. Values are reported from venous whole-blood (CBC and differential) and serum (CRP) specimens. Measurements outside the local laboratory reference intervals are indicated in bold. Peripheral blood eosinophilia was defined as eosinophils ≥5.0% of total leukocytes.

Patient	Age (years)	Gender	Diagnosis	Fever	WBC (×10^9/L)	Neutrophils (%)	Eosinophils (%)	Monocytes (%)	CRP (mg/L)	Severity	Prognosis
P1	10	M	Bronchoectasis	No	**2.16**	**36.0**	**0.1**	**10.7**	**5.7**	5	Poor
P2	13	M	Bronchial asthma	No	5.45	47.0	4.4	6.0	**12.0**	1	Neutral
P3	7	F	Bronchial asthma	No	**14.13**	42.5	**6.2**	4.0	0.8	2	Neutral
P4	6	M	Bronchoectasis	No	4.96	50.9	1.2	5.8	**6.5**	1	Neutral
P5	11	M	Bronchitis	**Yes**	5.99	50.3	4.6	9.0	**44.7**	3	Poor
P6	8	F	Bronchoectasis	No	7.53	53.6	2.3	7.0	2.9	0	Good
P7	16	F	Bronchial asthma	No	**4.33**	58.4	2.0	4.7	0.8	1	Neutral
P8	12	F	Bronchoectasis	No	7.36	43.8	3.4	7.3	1.0	0	Good
P9	14	M	Bronchial asthma	No	**4.34**	46.2	**0.7**	7.0	4.2	2	Neutral
P10	7	F	Bronchial asthma	No	7.87	45.6	4.6	5.9	**10.5**	1	Neutral

 doi:10.20944/preprints202603.1206.v1

Eosinophil levels were specifically evaluated, as they serve as a primary biomarker for Type 2 (T2) allergic airway inflammation [67–70]. Following standard clinical guidelines, peripheral blood eosinophilia was defined as an eosinophil fraction of ≥ 5.0% of total leukocytes. In the context of respiratory pathologies, exceeding this threshold typically indicates an allergic endotype, which often correlates with increased airway hyperresponsiveness and a higher likelihood of responding to corticosteroid therapy. True clinical eosinophilia was detected in only one participant (P3, 6.2%), corresponding directly with their diagnosis of bronchial asthma. Conversely, distinct eosinopenia (< 1.0%) was observed in P1 and P9. While patients P2, P5, and P10 exhibited eosinophil fractions at the upper limit of the normal range (4.4%–4.6%), they did not cross the clinical threshold for definitive eosinophilia.

To complement these systemic peripheral blood profiles, we next focused on the local pulmonary immune response. Specifically, the following section investigates the interaction between carbohydrate-functionalized fluorescent ligands (L1–L5) and alveolar macrophages derived from BALF.

2.4. Example Profiles of Ligand Binding Patterns in BALF Macrophages: Clinical Prognoses and Doxycycline Modulation Effects

The application of carbohydrate-functionalized fluorescent ligands to clinical BALF samples provided a functional readout of alveolar macrophage states, extending significantly beyond the capabilities of conventional cytomorphology. These ligand-binding patterns reflect the functional status of specific carbohydrate-recognition domains, which differ markedly among M0, M1, and M2a phenotypes. To translate these cumulative fluorescence signals into quantitative biological metrics, we employed a linear least squares deconvolution approach. This method models each patient's BALF profile as a proportional combination of established reference signatures: M0 (unpolarized), M1 (pro-inflammatory), and M2a (pro-resolving/allergic), as validated in our previous work.

Crucially, this analysis yields the relative contribution of each primary phenotype alongside a "residual" fraction, which captures any variance not explained by these three canonical reference states. This residual fraction effectively accounts for marginal or atypical macrophage subpopulations—including the M2b (immune-regulatory), M2c (immunosuppressive), and M2d (angiogenic) subtypes, as well as tumor-associated macrophages (TAMs). Because these alternative polarization states play a peripheral role in the specific, non-malignant respiratory diseases investigated here, aggregating them within the residual fraction maintains the model's focus on the dominant disease-driving M1/M2a axis without losing underlying sample complexity.

To test the clinical sensitivity of this method, we examined BALF macrophages from three pediatric patients with distinct diagnoses and outcomes: P1 (bronchiectasis, poor prognosis), P6 (bronchiectasis, good prognosis), and P7 (bronchial asthma, neutral prognosis) (Figure 3). Patient P1 (bronchiectasis, poor prognosis, Figure 3a) presented with severe systemic inflammation, leukopenia, and elevated C-reactive protein. The BALF macrophage compartment was strongly M1-dominated (66%) with negligible M0 and M2a fractions (<1% each), while ligand binding to L1–L5 was largely suppressible by mannan, indicating high engagement of dysregulated carbohydrate-recognition receptors such as CD206. The relatively low residual component (32%) is consistent with a rigid, highly polarized inflammatory state.

In contrast, Patient P6 (bronchiectasis, good prognosis, Figure 3c) showed milder systemic inflammation and normal leukocyte counts, yet still exhibited an M1-biased profile (57%). Here, however, the residual fraction was markedly higher (41%), suggesting preserved phenotypic plasticity and the presence of intermediate or transitioning macrophage states, which aligns with the more favorable clinical trajectory. Patient P7 (bronchial asthma, neutral prognosis, Fig, 3e) displayed a qualitatively different pattern, with a predominant M2a contribution (38%) and substantial residual (43%), in line with the alternative activation and tissue-remodeling programs characterizing Th2-driven asthma rather than acute bacterial infection.

 doi:10.20944/preprints202603.1206.v1

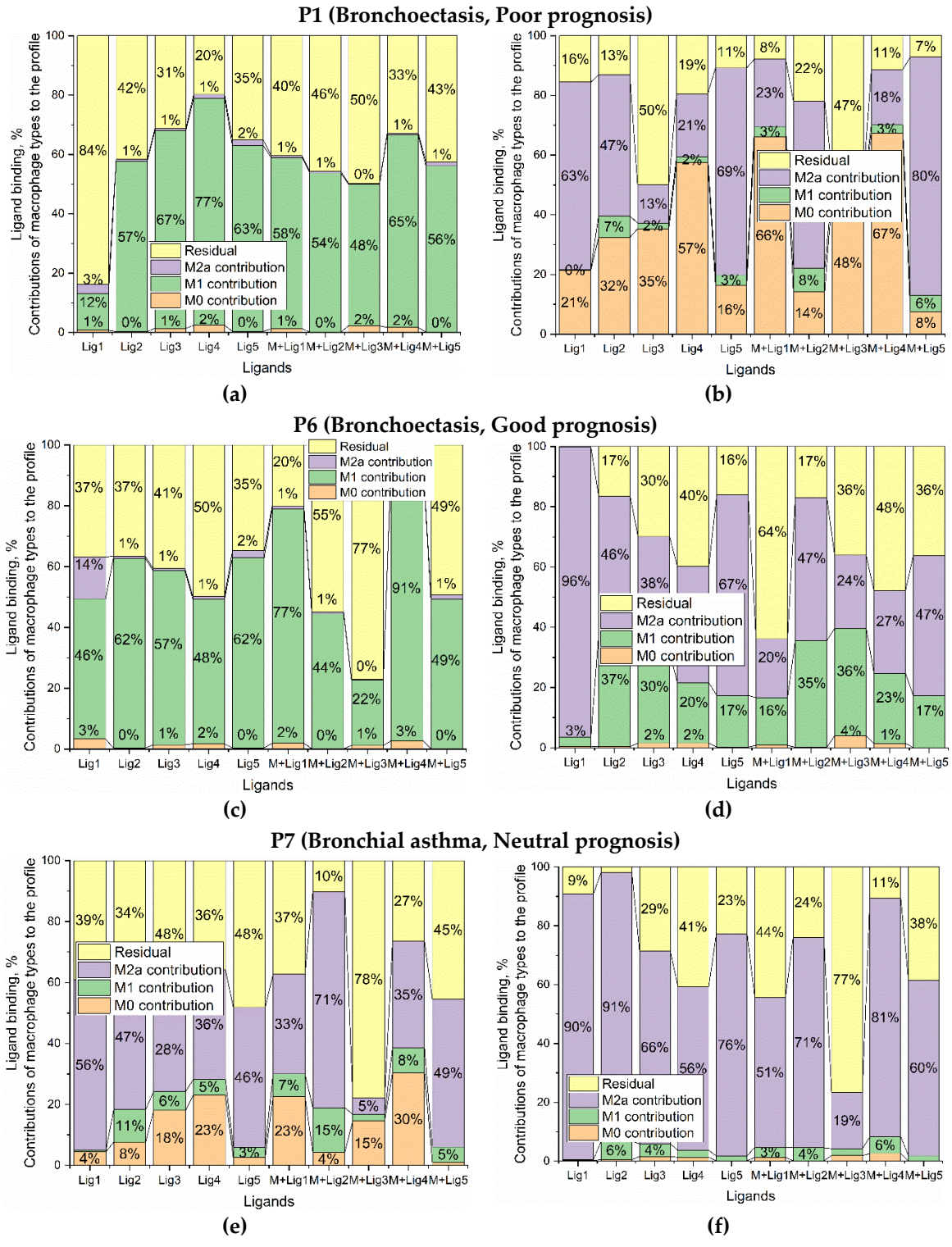

Figure 3. Ligand binding profiles of BALF macrophages in pediatric respiratory disease patients before and after doxycycline treatment. **a**, **b**, Phenotype contributions in Patient P1 (bronchiectasis, poor prognosis) at baseline (**a**) and following doxycycline treatment (**b**). **c**, **d**, Phenotype contributions in Patient P6 (bronchiectasis, good prognosis) at baseline (**c**) and following doxycycline treatment (**d**). **e**, **f**, Phenotype contributions in Patient P7 (bronchial asthma, neutral prognosis) at baseline (**e**) and following doxycycline treatment (**f**). Vertical stacked bar charts display the relative percentage of each phenotype across five carbohydrate-functionalized fluorescent probes (Lig1–Lig5). Data for competitive binding assays with mannan are labeled as M+Lig1 to M+Lig5. Color coding represents deconvoluted phenotype contributions: orange, M0; green, M1; purple, M2a; yellow, residuals (other macrophages subtypes). Percentage values within the bars indicate the calculated contribution of each reference phenotype to the respective BALF sample.

 doi:10.20944/preprints202603.1206.v1

To determine if this profiling framework could capture dynamic phenotypic shifts in response to pharmacological stimuli, we evaluated the effects of a clinically used antibiotic (Figure 3b, d, f). Specifically, ex vivo BALF macrophages were treated with doxycycline (0.1 mg/mL). Doxycycline was selected because it is a broad-spectrum tetracycline frequently prescribed for respiratory infections, and importantly, it possesses known immunomodulatory properties [49,50]. Within our developed test system and BALF macrophage model, doxycycline served as an ideal model compound to verify whether ligand-based deconvolution can effectively resolve drug-induced macrophage repolarization.

Across all three patients, doxycycline consistently suppressed the M1 component and enhanced M2a contributions, but the functional implications differed sharply depending on the baseline state (Figures 3 bdf and 4). In the severe bronchiectasis case P1, doxycycline triggered a profound shift: the pathological M1 fraction collapsed from 66% to 4%, while M0 and M2a fractions increased to 51% and 36%, respectively. This pattern resembles a "reset" of the inflammatory compartment, restoring a pool of resident-like cells and activating reparative programs, which could be beneficial in sepsis-like hyperinflammation. In the milder bronchiectasis case P6, doxycycline promoted a more targeted transition from M1 (57% to 27%) toward M2a (1% to 49%) without accumulating an intermediate M0 pool, consistent with efficient engagement of resolution pathways in a system with intact regulatory capacity.

Conversely, in asthma patient P7, doxycycline exacerbated a preexisting M2a-skewed environment, increasing the M2a fraction to 80% while significantly reducing overall population heterogeneity. Because M2-like alveolar macrophages are known drivers of airway remodeling and fibrosis in chronic asthma, reinforcing this M2a polarization could risk aggravating structural lung damage rather than conferring a therapeutic advantage. Furthermore, doxycycline treatment universally reduced the residual macrophage fraction across all patients (decreasing to 9–23%). This shift suggests a drug-induced "phenotypic consolidation," where previously intermediate or undefined cellular states are driven into established M0, M1, or M2a programs—heavily biased toward M2a. Together, these observations highlight the critical need for personalized profiling systems to screen and select antibiotics that are safe and appropriate for a patient's unique microenvironment.

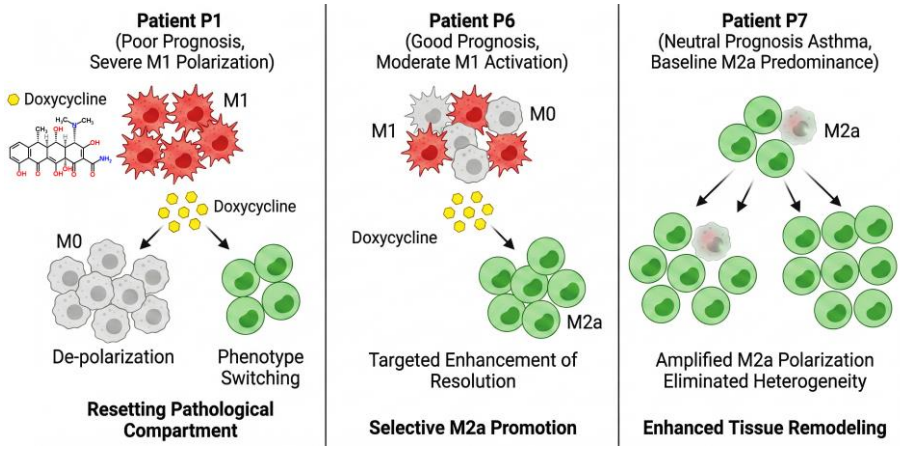

Figure 4. Doxycycline-induced macrophage phenotype responses in three pediatric respiratory disease patients. Schematics depict baseline BAL macrophage composition (top) and post-doxycycline (0.1 mg/mL) phenotype distribution (bottom) for each patient. Patient P1 (poor prognosis, bronchiectasis): baseline M1-dominant state transitions to M0-enriched and M2a-shifted phenotypes. Patient P6 (good prognosis, bronchiectasis): moderate baseline M1 activation selectively shifts toward M2a polarization with retained M0 components. Patient P7 (neutral prognosis, asthma): baseline M2a-predominant state intensifies to near-homogeneous M2a distribution with reduced heterogeneity. Doxycycline molecule (structural formula shown) indicates the exposure condition. Color coding: gray = M0 (resident), red = M1 (pro-inflammatory), green = M2a (resolution/remodeling).

 doi:10.20944/preprints202603.1206.v1

Collectively, these case studies highlight the dual nature of pharmacological immunomodulation (Figure 4). While doxycycline serves as a potent switch—dampening M1-driven inflammation in favor of M2a-associated resolution—the clinical benefit of this shift depends heavily on the baseline immune microenvironment. For instance, this repolarization offers therapeutic potential in M1-dominated bronchiectasis (P1, P6) but risks being maladaptive in M2a-biased asthma (P7). Consequently, our ligand-based BALF macrophage phenotyping emerges as a promising companion diagnostic tool. By distinguishing patients who would benefit from M1-suppressive treatments from those at risk of treatment-induced complications like asthma exacerbations or fibrosis, this framework paves the way for personalized immunomodulatory interventions in respiratory medicine.

2.5. Ex Vivo Screening of Compounds for Remodeling Macrophage Functional States in Patient BALF

Building on the distinct ligand binding profiles associated with varying clinical prognoses and the modulatory effects of doxycycline (Section 2.4), we next investigated the targeted reprogramming of macrophage functional states via ex vivo screening of a compound library. This transition from descriptive phenotyping to an interventional strategy allows for the direct identification of pharmacological agents that can shift patient-derived macrophages toward beneficial, anti-inflammatory M2-like phenotypes.

The analysis of intact (untreated) alveolar macrophages revealed profound inter-patient variability, providing a cellular explanation for why standardized treatments often yield inconsistent clinical results. As detailed in Table S1 and Figure 5, the baseline distribution of macrophage phenotypes differed significantly across the cohort ($p < 0.01$). Patients P1 and P4, associated with chronic inflammatory conditions like bronchiectasis, exhibited a baseline phenotype heavily skewed toward the pro-inflammatory M1 state, with contributions of 66% and 66%, respectively. In these patients, the M1 fraction was significantly higher than the M0 or M2a fractions ($p < 0.01$), suggesting a "locked-in" inflammatory profile. In sharp contrast, patients P3 and P8 presented with a "quiescent" profile dominated by unactivated M0 cells (44% and 59%, respectively) or mixed residual phenotypes, with negligible M1 activity (<18%). This baseline divergence ($p < 0.001$ between P1 and P3 M1 levels) implies that while P1 might require immune dampening, P3 likely requires stimulation—a nuance lost in standardized protocols.

To test the potential for immune reactivation in quiescent phenotypes, we examined the effects of 4-Methylumbelliferone (MUmb). Based on its structural classification as a coumarin derivative—a scaffold known for immunostimulatory properties—we hypothesized that MUmb would effectively polarize dormant M0 cells into an active M1 state. The data provided a robust statistical validation of this hypothesis. In Patient P3, whose intact macrophages were largely dormant (44% M0, 1% M1), incubation with MUmb triggered a massive functional inversion, surging the M1 contribution to 74% (Table S1). This increase was highly significant ($p < 0.001$ compared to untreated control), effectively "waking up" the previously dormant immune cells. A similar reinforcement of the M1 phenotype was observed in Patient P6, where the M1 fraction rose from 57% to 84% ($p < 0.01$), and in Patient P1, where it increased from 66% to 77% ($p < 0.05$). These results confirm that coumarin-based agents can significantly override baseline dormancy, offering a statistically viable strategy for patients with "cold" immune responses.

Conversely, for patients exhibiting hyper-inflammatory baselines, the therapeutic goal is to shift the phenotype toward M0 (resolution) or M2a (tissue repair). Here, the screening highlighted the unique efficacy of Doxycycline as a reprogramming agent. In Patient P1, who started with a critically high inflammatory load (66% M1), Doxycycline treatment practically abolished M1 expression, reducing it to just 4% ($p < 0.001$). Concurrently, we observed a significant compensatory increase in the M0 (51%) and M2a (36%) populations, confirming a successful reprogramming event rather than mere cell death. Even more striking was the response in Patient P7, where Doxycycline drove an 80% shift toward the anti-inflammatory M2a phenotype, a statistically significant deviation from the

 doi:10.20944/preprints202603.1206.v1

baseline of 38% ($p < 0.01$). This contrasts sharply with other agents like Paclitaxel, which generally maintained the pre-existing M1 profile (e.g., P4 maintained 69% M1, $p > 0.05$ vs. intact) or failed to induce significant remodeling.

This ex vivo platform effectively functions as a "drug sensitivity assay" for the immune system. This represents a foundational step toward moving beyond generic protocols to a truly personalized immunotherapy for respiratory pathology.

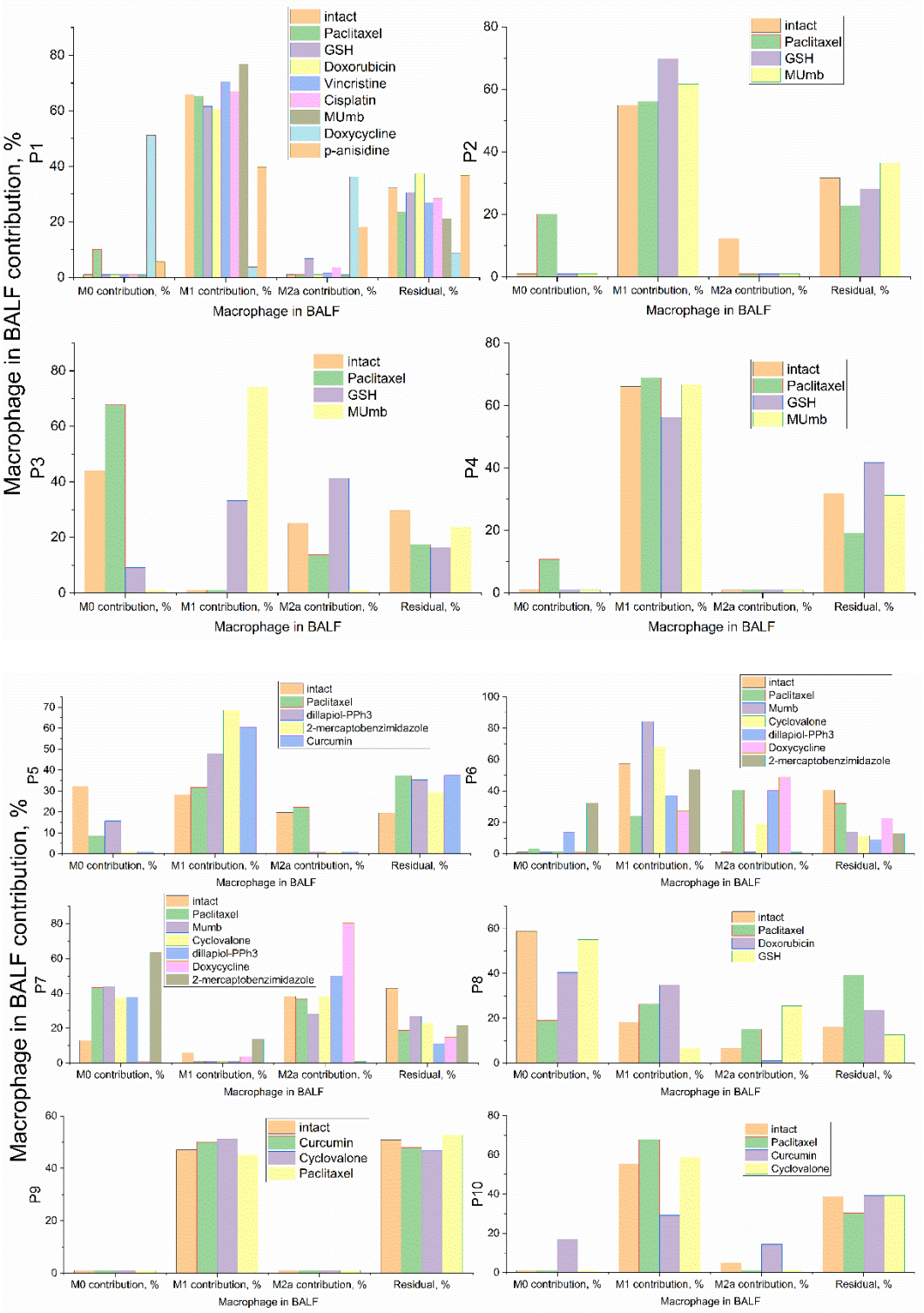

Figure 5. Individual remodeling of macrophage functional states in patient BALF. Bar charts illustrate the percentage contribution of M0 (unactivated), M1 (pro-inflammatory), M2a (anti-inflammatory/repair), and

 doi:10.20944/preprints202603.1206.v1

Residual classes for each patient under "intact" conditions and following incubation with various bioactive substances.

2.6. Statistical Validation and Diagnostic Applicability of Pharmacological Remodeling

To quantify the immunomodulatory potential of the tested library across the patient cohort, we analyzed the remodeling delta (Δ, %), defined as the net shift in phenotype contribution between treated and intact states (Figure 6).

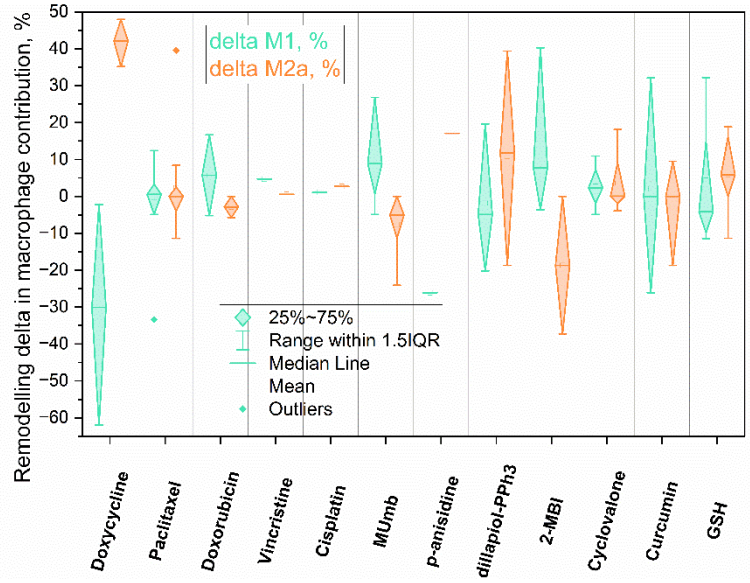

Figure 6. Statistical analysis of macrophage remodeling capacity. Violin and box plots representing the distribution of changes (delta, %) in M1 (green) and M2a (orange) contributions relative to the intact state across the patient cohort. The box indicates the interquartile range (IQR), the horizontal line represents the median, and the small square represents the mean.

Using least-squares deconvolution and pattern recognition of patient-derived BALF cell profiles against established M0, M1, and M2a reference populations, our ex vivo platform translates complex repolarization events into a measurable net clinical vector (Table 3). Instead of treating all agents as a monolith, our analysis segregates the compounds into three distinct functional and pharmacological categories: antibiotics, cytostatics, and immunomodulatory adjuvants.

Table 3. Comprehensive classification of the tested pharmacological and biologically active agents based on their macrophage remodeling direction. Phenotypic shifts were quantified utilizing least squares deconvolution of patient-derived BALF cells profiles against established reference M0, M1 and M2a populations.

Substance Class	Agent	Predominant effect	Physiological interpretation
Antibiotics	Doxycycline 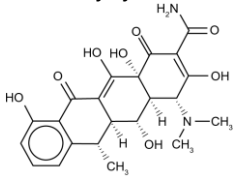	Strong M2a Polarization (e.g., P7).	High potential for resolving chronic inflammation; however, poses a risk of exacerbating fibrosis in Th2-driven conditions (e.g., asthma).
Cytostatics	Paclitaxel	M0 Shift (Deactivation). Increases marker-	Disruption of polarization signaling; cellular "reset" or

 doi:10.20944/preprints202603.1206.v1

	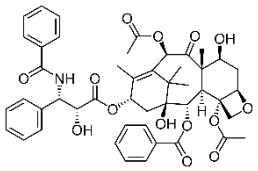	negative population.	immune tolerance breaking due to cytoskeletal stress.
	Vincristine 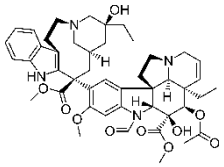	Slight increase in M1 (e.g., P1).	Pro-inflammatory modulation alongside cytotoxic effects; risks sustaining sterile inflammation.
	Doxorubicin 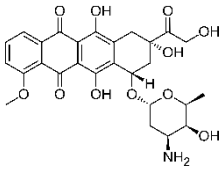	M1/M0 Mixed. Shifts M0 to M1 (e.g., P8) or maintains M1.	Induction of immunogenic cell stress and acute pro-inflammatory signaling.
	Cisplatin 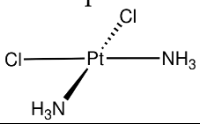	M1 Maintenance. Maintains high inflammatory profile.	Preservation of the chronic inflammatory state under severe cellular stress.
Pharmaceuticals (Modulators) & Adjuvants	Cyclovalone 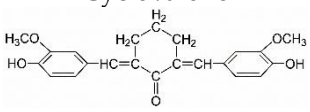	Moderate M2a induction (P6).	Weak modulator with highly variable individual patient responses.
	MUmb (4-Methylumbelliferone) 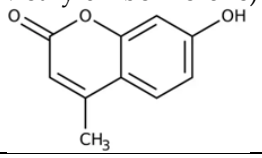	M1 Polarization. Induces M1 from M0 (e.g., P3); stabilizes high M1.	Macrophage activation; potential utility as an adjuvant in cancer immunotherapy to heat up “cold” tumors.
	2-mercaptobenzimidazole (2-MBI) 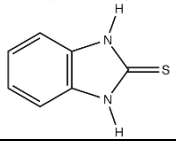	Strong M1 induction (P5) or M0 shift (P7).	High variability suggests toxicity or stress-response-mediated alternative activation.
	p-anisidine 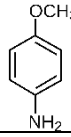	M2a shift. Reduced M1, increased M2a (P1).	Partial shift towards a tissue-repair phenotype in states of severe inflammation.
	Dillapiol-PPh^3 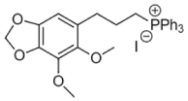	Moderate M2a shift (P6, P7).	Mild anti-inflammatory activity; potential redox modulation driving resolution.
Nutraceuticals & Metabolites	Curcumin 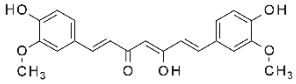	Context-Dependent. Mainly Decreased M1 (P10).	Adaptogenic effect; outcome depends heavily on the baseline immune status of the patient.
	GSH (Glutathione)	Redox Support.	Supports cell viability; effect largely mirrors the

 doi:10.20944/preprints202603.1206.v1

	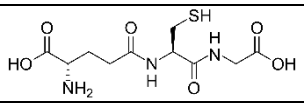		dominant baseline phenotype.

2.6.1. Antibiotics Secondary Effects

Doxycycline acted as the strongest directional driver in the library. It produced a significant negative ΔM1 (entire IQR below zero, $p < 0.001$) with a concurrent increase in M2a ($p < 0.01$), exemplified by $\Delta \approx -60\%$ M1 in Patient P1 and up to 80% M2a in Patient P7. Although doxycycline is reported to inhibit IL-4/IL-13-induced M2 polarization in isolated cell-line models, native alveolar macrophages in our BALF-based assay consistently shifted toward a reparative M2a state. This divergence highlights the gap between standardized in vitro conditions and the cytokine milieu of patient-derived material, and directly supports the rationale for ex vivo functional testing

The pronounced M2a-promoting effect of doxycycline illustrates how the same antibiotic can be beneficial or harmful depending on the patient's immune context. In Th2-dominated allergic conditions (asthma) — where IL-4- and IL-13-driven responses already skew the microenvironment toward a maladaptive M2 phenotype — an M2a-promoting antibiotic may exacerbate airway remodeling and fibrosis. In chronic M1-driven inflammation (bronchiectasis), the same compound becomes therapeutically desirable as a resolution driver. Detecting this duality at the individual level is precisely the purpose of the test system.

2.6.2. Cytostatics Secondary Effects

The four tested cytostatics produced markedly different secondary immunomodulatory signatures.

Paclitaxel stood apart by shifting macrophages toward the marker-negative M0 state — a functional passivation rather than true de-differentiation, which is not possible for committed macrophages. Low-dose paclitaxel is known to promote M1 polarization via TLR4/NF-κB signaling, yet in our system the dominant effect was suppression of polarization markers, likely driven by cytoskeletal disruption and STAT3 inhibition. The ΔM2a variance across patients was high ($p > 0.05$), confirming that paclitaxel is a context-dependent modulator whose net outcome depends on the patient's baseline.

Doxorubicin shifted the macrophage profile toward an M1 state with a reduction in M2a, this effect is profoundly dose- and context-dependent. As highlighted in our previous work [38], doxorubicin can promote M2 polarization, thereby activating tumor-associated macrophages (TAMs) and provoking secondary metastasis. We further corroborated this context-dependency in our own experiments using specific doxorubicin formulations, which notably triggered an M2-promoting effect. These findings vividly illustrate the importance of drug formulation; the delivery vehicle alone can dictate a drug's secondary immunomodulatory direction. Consequently, while modifying drug formulations offers a powerful strategy to intentionally guide immune responses, these off-target effects remain patient and dose-specific. To ensure therapeutic safety and efficacy, personalized ex vivo testing of these formulations is absolutely essential.

Vincristine and cisplatin exerted minimal net effect on macrophage phenotype. Their violin distributions were clustered near zero for both ΔM1 and ΔM2a, indicating that at the tested concentrations these agents do not substantially remodel the macrophage landscape. This absence of a secondary immunomodulatory signal is itself diagnostically relevant, distinguishing vincristine and cisplatin from doxorubicin and paclitaxel as agents with lower risk of off-target immune perturbation.

2.6.3. Adjuvants and Small Molecules as Context-Dependent Modulators

4-Methylumbelliferone (MUmb), a coumarin-based hyaluronan synthesis inhibitor, was the most consistent immunostimulant. ΔM1 showed a tightly clustered positive shift ($p < 0.05$), in line with its reported ability to polarize macrophages toward an M1 profile and potentiate antitumor

 doi:10.20944/preprints202603.1206.v1

immunity. In our test system, MUmb represents a compound capable of activating quiescent macrophages — a key property for reversing immuno- silence what is referred to as a problem in pulmonary tuberculosis.

Curcumin exhibited a pronounced bidirectional immunomodulatory profile: it attenuated the M1 phenotype in patients with a high inflammatory baseline (e.g., P10) while paradoxically promoting M1 polarization in those with lower baseline inflammation (e.g., P5). This aligns with recent findings highlighting the complex, pleiotropic effects of turmeric-derived compounds on macrophages; for instance, Curcuminoids have been shown to simultaneously downregulate M1 surface markers (CD86) and upregulate M2-associated markers (CD163, IL-10, TGF-β), while actively enhancing the expression of antibacterial pro-inflammatory cytokines (IL-1β, IL-6, TNF-α) [71]. C**yclovalone**—a synthetic curcuminoid characterized by cyclooxygenase-inhibitory activity—elicited only weak and variable modulation, driving moderate M2a induction in a subset of patients while merely maintaining the M1 phenotype in others.

2-Mercaptobenzimidazole (2-MBI), a benzimidazole derivative with documented antimicrobial and analgesic properties, demonstrated a highly context-dependent effect. Specifically, we observed strong M1 induction in certain patient profiles (e.g., P5), contrasting with a shift toward an unpolarized M0 state in others (e.g., P7). This divergence suggests a narrow therapeutic window between active immunostimulation and stress-induced macrophage passivation. In contrast, p-Anisidine and Dillapiol-PPh3—a mitochondria-targeted terpenoid–triphenylphosphonium conjugate previously characterized by our group [72]—consistently promoted an M2a phenotypic shift, firmly positioning them as candidate anti-inflammatory adjuvants.

Glutathione (GSH) exhibited behavior that largely mirrored the dominant baseline phenotype of the patient, acting primarily as a redox buffer rather than a directional polarization driver. In the literature, intracellular GSH levels are recognized as critical for macrophage function [34]: elevated GSH typically supports M1-mediated cytotoxicity and antigen presentation, whereas its depletion is heavily associated with M2 polarization and immunosuppression, a mechanism frequently exploited by tumor-associated macrophages (TAMs) in oncology. However, our findings indicate that in the context of respiratory pathology, exogenous GSH application restores redox homeostasis without forcing a specific phenotypic shift. This makes GSH a highly promising, safe synergistic adjuvant; for instance, in routine respiratory infections like bronchitis, it can alleviate oxidative stress without the risk of abruptly dampening necessary antimicrobial (M1) clearance mechanisms or exacerbating hyperinflammation.

To sum up, the evaluation of this adjuvant class highlights the platform's potential for rational, disease-specific combination design. The literature establishes that distinct clinical scenarios require fundamentally opposing immunomodulatory strategies. For example, allergic asthma and early-stage severe pneumonia demand the resolution of hyperinflammation, whereas oncology or post-infectious immunoparalysis require robust macrophage activation. Our ex vivo findings align directly with these targeted clinical needs: MUmb consistently activated macrophages toward an M1 phenotype, making it an excellent candidate for reversing immunoparalysis in late-stage pneumonia. Conversely, **p-anisidine** and **Dillapiol-PPh$_3$** promoted M2a polarization, rendering them highly suitable for resolving hyperinflammation in asthma or acute lung injury. Curcumin's response remained entirely context-dependent, necessitating personalized screening, while GSH served as a universally safe redox support.

This stratification carries a profound practical implication: drugs within the same therapeutic class may exert opposite secondary effects on macrophage polarization. A pneumonia patient trending toward life-threatening hyperinflammation requires a fundamentally different immunomodulatory accompaniment than one suffering from immunoparalysis, even if both receive the identical empirical antibiotic regimen. Our platform identifies these divergent clinical trajectories, providing a rational basis for selecting adjuvants or formulations that steer the net immune response in the desired direction—ultimately shifting treatment from empirical antimicrobial eradication toward precision immune synchronization.

 doi:10.20944/preprints202603.1206.v1

2.6.4. The Translational Bridge to Precision Immunology

Recent comprehensive studies [25] have employed highly complex, multi-method approaches to map how specific macrophage subpopulations (such as pro-fibrotic CCRL2+ or reparative CD160+ cells) shift during acute inflammation in organs like the liver or heart. However, the sheer volume of high-dimensional data generated by these techniques often creates a convoluted and overwhelming picture. Rather than yielding clear, actionable insights, this hyper-granularity makes it exceedingly difficult to extract straightforward, practical conclusions that can be directly applied to bedside decision-making.

Our ex vivo test platform provides a vital, rapid alternative: tracking the immunomodulatory vector via functional pattern deconvolution. Because a primary therapy (like an antibiotic or cytostatic) can have contradictory immune side-effects depending on the patient's baseline context, empirical treatment is no longer sufficient. By utilizing this diagnostic platform, clinicians can proactively identify whether a patient is heading toward hyper-inflammation or immunoparalysis. Consequently, primary therapies can be precisely "complemented" with targeted adjuvants or specific formulations to correct the immune trajectory, shifting the paradigm from simple pathogen eradication to personalized immune synchronization.

2.7. Multivariate Linear Discriminant Analysis Reveals Distinct Ligand-Binding Signatures Correlated with Disease Severity

The preceding functional profiling established that pharmacological remodeling is inherently context-dependent, where a single agent may resolve inflammation in one host while exacerbating pathology in another depending on the baseline immune status. Consequently, the critical translational challenge lies in differentiating patients to identify who will benefit from remodeling versus those at risk. To address this, we moved beyond individual markers to a multivariate mathematical approach capable of decoding the global landscape of macrophage-ligand interactions. We applied Linear Discriminant Analysis (LDA) to aggregated ligand-binding data from a diverse cohort of 72 patients presenting with distinct respiratory pathologies. This model was trained to segregate the population into "Good," "Neutral," and "Poor" prognostic cohorts using a composite severity index derived from standard leukocyte parameters and C-reactive protein levels (Figure 7).

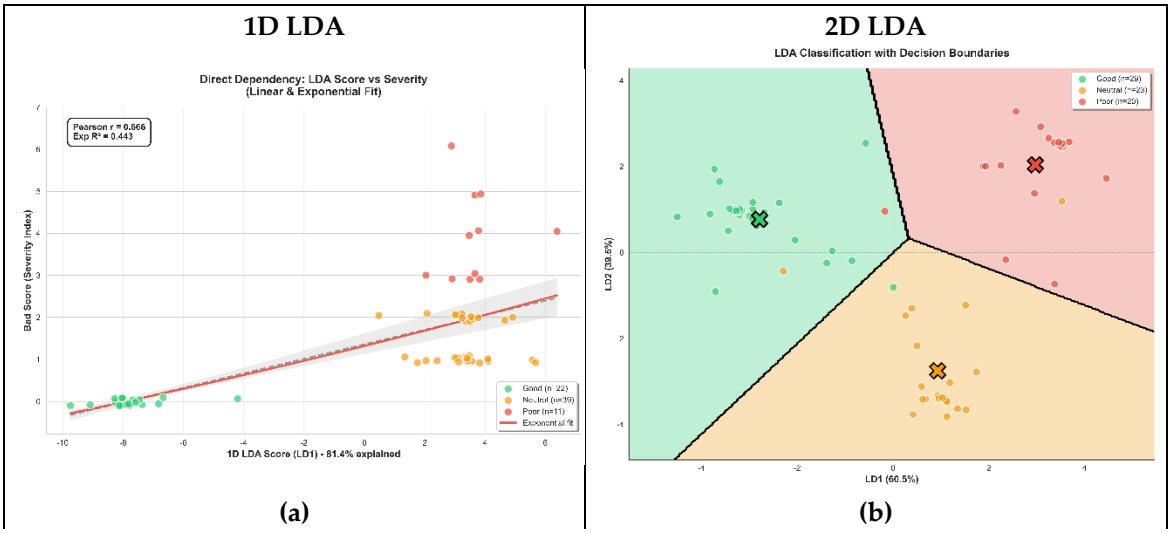

Preprints.org (www.preprints.org) | NOT PEER-REVIEWED | Posted: 17 March 2026 doi:10.20944/preprints202603.1206.v1

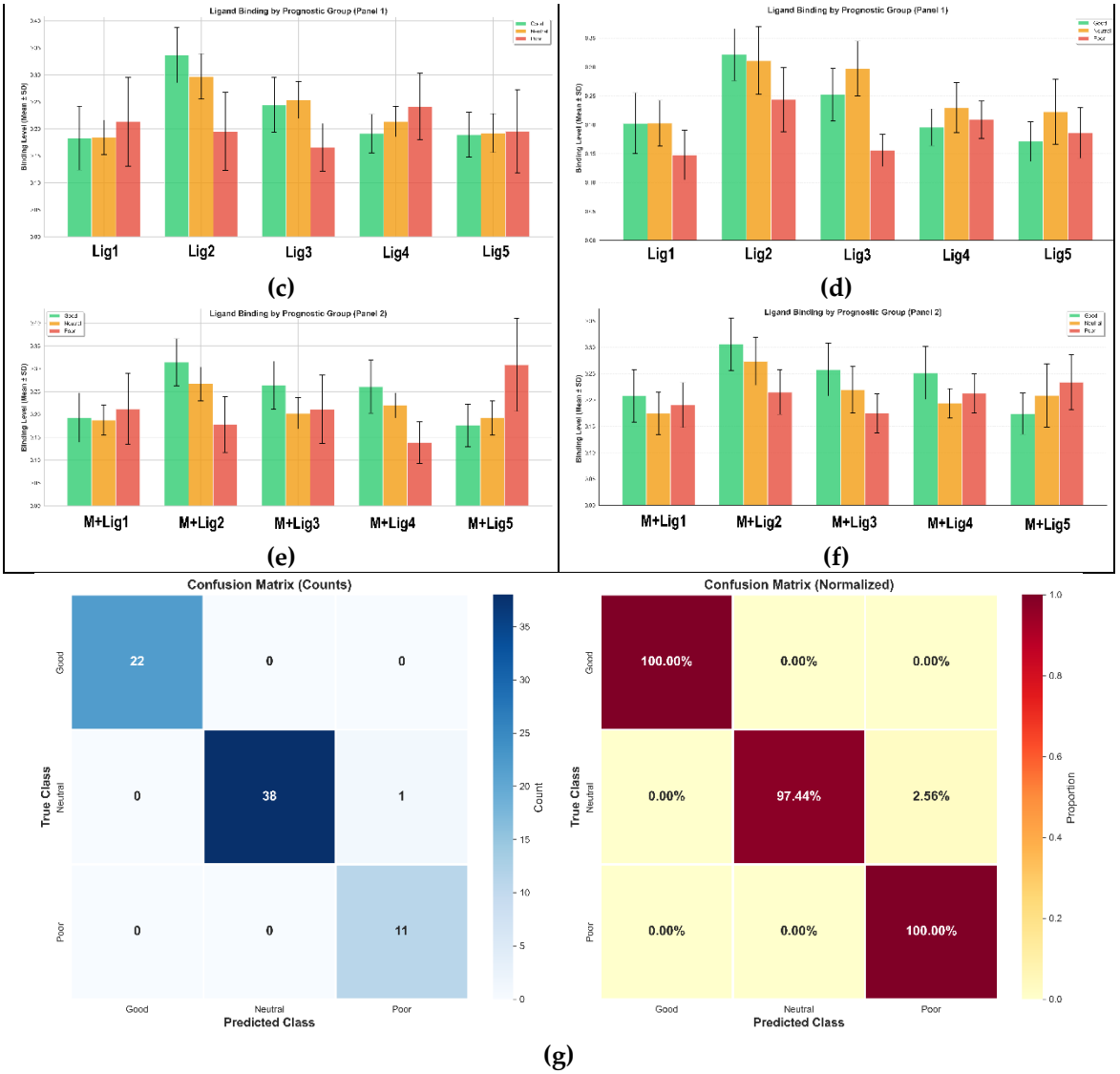

Figure 7. Linear discriminant analysis of BALF cells ligand binding profiles. **(a)** Correlation analysis between the 1D LDA Score (LD1) and the clinical Severity Index. The regression line (red) with confidence intervals (grey) reveals a strong dependency (Pearson $r = 0.666$). **(b)** 2D projection of the LDA showing distinct clustering. **(c–f)** Raw ligand binding levels (Mean ± SD) for individual ligands (Panel 1) and Mannan-inhibited conditions (Panel 2): (c, e) for 1D LDA; (d, f) for 2D LDA. **(g)** Confusion matrices displaying classification performance.

The resulting classification performance was highly robust, as evidenced by the confusion matrices (Figure 7g). The model achieved high sensitivity for the extreme phenotypes, correctly identifying all patients in the "Good" (n=22) and "Poor" (n=11) categories, with only a single misclassification occurring in the "Neutral" group (97.44% accuracy). This statistical separation is visually represented in the two-dimensional canonical space (Figure 7b), where the first linear discriminant (LD1) captures 60.5% of the variance. The topological distribution within this space is clinically revealing: the "Good" prognosis group (green) forms a tight, cohesive cluster. This does not necessarily represent a naive homeostatic baseline, but rather a distinct, regulated immune state indicative of a correct therapeutic trajectory and a high probability of recovery. In sharp contrast, the "Poor" prognosis group (red) exhibits significant spatial dispersal. This loss of clustering density reflects high phenotypic heterogeneity, suggesting that severe pathology is characterized not by a single resistant phenotype, but by a chaotic loss of immune regulation and a drift into stochastic dysregulation.

 doi:10.20944/preprints202603.1206.v1

Crucially, the LD1 axis functions as more than a categorical classifier; it serves as a continuous biological meter of macrophage dysfunction. As shown in the regression analysis (Figure 7a), there is a significant positive correlation (Pearson r = 0.666) between the LD1 score and the clinical Severity Index. The relationship is best described by an exponential fit (R^2 = 0.443), implying that as the macrophage phenotype deviates from the favorable therapeutic zone (increasing LD1), clinical deterioration does not merely increase linearly but accelerates. This suggests that the LD1 score captures the underlying biological substrate of disease progression before it manifests as catastrophic clinical failure.

To decode the molecular drivers of this classification, we examined the raw and inhibited ligand binding profiles (Figure 7c–f). The bar charts illustrate distinct binding signatures across the three groups for both native conditions (Panel 1) and Mannan-inhibited conditions (Panel 2, labeled M+Lig). Notably, the feature importance hierarchy indicated a dominance of inhibition by mannan terms. This points to the functional integrity of the Mannose Receptor (CD206) as a primary discriminator. Unlike standard antibody staining, which provides a binary "digital" signal (presence/absence), our library of medium-affinity ligands generates a nuanced "analog" readout of receptor functionality.

In patients with favorable prognoses, binding profiles reflect specific, high-affinity interactions that respond effectively to inhibitors (Figure 7c, e). In contrast, "Poor" prognosis patients lose this specificity. The aberrant levels in these cohorts (Figure 7d, f), especially in the inhibited state, indicate non-specific uptake or receptor saturation refractory to competitive inhibition. Consequently, the macrophage binding profile acts as an early warning biomarker: high LD1 scores warrant aggressive monitoring or treatment adjustments regardless of mild clinical symptoms. Finally, this model provides a quantifiable therapeutic target. Because macrophage modulation inherently drives the suppression of corresponding cytokines, successful intervention cannot be measured by cytokine reduction alone. Instead, treatment must physically reposition the patient's macrophage state on the canonical LDA plot, moving it from the dysregulated "red" zone into the "green" recovery cluster.

Having established the static topological landscape of disease severity, we advanced to the critical phase of the analysis: visualizing the dynamic shifts induced by therapeutic agents. By projecting the ex vivo remodeling data onto the canonical LDA space defined in Figure 7, we calculated the specific "therapeutic vector" generated by each compound. This approach effectively overlays pharmacological trajectories onto the patient's specific immune landscape, allowing us to determine whether a drug drives the macrophage population toward the homeostatic "Good" cluster or propels it further into the dysregulated "Poor" zone. This vector analysis is detailed in Figure 8, which contrasts the distinct pharmacological responses of two patients with divergent baseline statuses—Patient P3 (Neutral) and Patient P7 (Borderline/Poor).

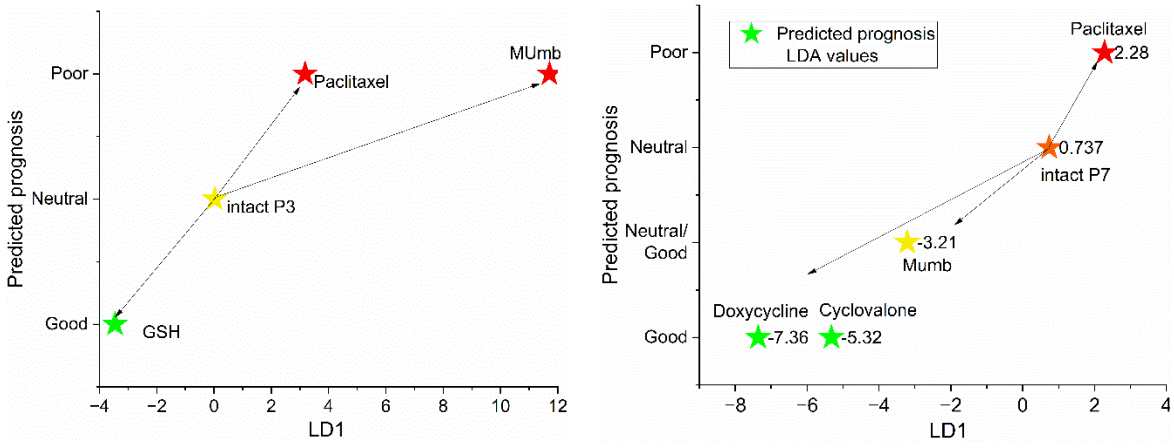

 doi:10.20944/preprints202603.1206.v1

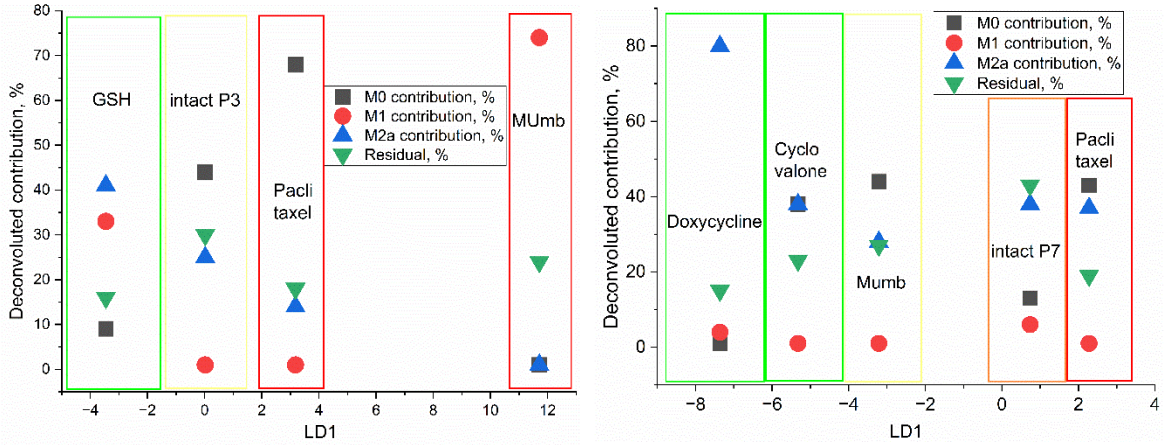

Figure 8. Vector analysis of pharmacological remodeling in patient-specific BALF cells populations. (a, b) Projection of ex vivo treated alveolar macrophages onto the canonical LDA space. Arrows indicate the magnitude and direction of the therapeutic vector from the intact state (start) to the remodeled state (end). Stars represent the predicted prognosis zone: Green (Good), Yellow (Neutral), Red (Poor). (a) Trajectories for Patient P3 (initially Neutral). (b) Trajectories for Patient P7 (initially Neutral/Poor). (c, d) Corresponding deconvoluted phenotype contributions (M0, M1, M2a) for the specific LD1 coordinates shown above for Patient P3 (c) and Patient P7 (d).

Importantly, our primary objective here is not to treat specific clinical conditions, such as bronchitis, but rather to utilize a highly tractable ex vivo model to ascertain how various pharmacological agents alter macrophage status and dictate clinical trajectories, be they favorable or unfavorable. Our findings demonstrate that this platform is exceptionally sensitive to these immunological shifts, establishing it as a robust tool for monitoring therapeutic efficacy and optimizing custom drug formulations.

The trajectory analysis for Patient P3 (Figure 8a) vividly illustrates the critical necessity of personalized screening. Initially positioned in the "Neutral" zone (LD1 ≈ 0), this patient's macrophages exhibited a robust restorative shift under the influence of the adjuvant Glutathione (GSH), which drove the vector deep into the "Green" prognostic zone (LD1 < –3). Phenotypically, this improvement correlated with a resurgence of the reparative M2a fraction and a suppression of the chaotic M0 population (Figure 8c). Conversely, evaluating other drug classes revealed divergent mechanisms of cellular deterioration. For instance, the immunomodulator MUmb provoked a massive, maladaptive spike in the pro-inflammatory M1 fraction, reaching up to 75%. While such a cytokine storm-like response would be therapeutically highly beneficial in contexts like tuberculosis or when targeting tumor-associated macrophages (TAMs), it drove this patient's vector sharply toward the "Poor" prognosis zone. Assessed separately, cytostatic agents also proved detrimental; Paclitaxel directed the vector toward the "Poor" zone by inducing functional paralysis, characterized by a dominant, marker-negative M0 phenotype.

A different therapeutic imperative emerged for Patient P7 (Figure 8b), whose baseline status was already severely compromised. Starting with antibiotic interventions, Doxycycline functioned as a highly potent "resolution driver." It generated a vector of significant amplitude (LD1 = –7.4) that successfully repositioned the cellular system within the "Good" cluster, a restoration underpinned by a decisive dominance of the M2a phenotype (Figure 8d, ~80%). Similarly, among the adjuvants, cyclovalone demonstrated a favorable, albeit less aggressive, corrective vector. However, looking at cytostatics independently, Paclitaxel once again confirmed its destabilizing potential (LD1 = 2.3), exacerbating the patient's existing dysregulation. Collectively, these data validate the LD1 axis as an integral biomarker: negative values signify immune consolidation, whereas positive values indicate an entropic drift toward aggression or functional inertia.

 doi:10.20944/preprints202603.1206.v1

To sum up, our study establishes a comprehensive framework for transitioning from empirical immunopharmacology to precision immune "engineering". We demonstrate that the concept of "universal" immunomodulators is a clinical fallacy; the efficacy of any agent is strictly vector-dependent, dictated by the interaction between the drug's mechanism and the patient's unique ligand-receptor landscape. The integrated platform presented here, combining high-content ex vivo bioimprinting with multivariate mathematical modeling, seamlessly addresses three fundamental clinical needs. First, it enables diagnostic stratification by detecting patients with a "latent Poor" prognosis before clinical decompensation occurs. Second, it facilitates personalized screening to filter out agents that, despite general efficacy, would trigger catastrophic off-target polarization in a specific host—as evidenced by the MUmb-induced inflammatory shift in Patient P3's specific pathology. Finally, it permits the rational design of combination therapies, such as pairing cytostatic agents with specific adjuvants to counterbalance therapeutic toxicity and realign the immune vector. Ultimately, the implementation of this predictive navigation system moves the field beyond standardized protocols toward a mathematically rigorous strategy of individualized immune recovery.

3. Materials and Methods

3.1. Reagents

Polyethyleneimine (PEI, MW 1.8 kDa) was purchased from Sigma-Aldrich (St. Louis, MO, USA). Carbohydrates, including mannan, α-D-mannose (Man), methyl-α-D-mannoside (Me-Man), D-galactose, and D-lactose, were obtained from Sigma-Aldrich (St. Louis, MO, USA). Mannotriose-di-(N-acetylglucosamine) (triMan-GlcNAc) was obtained from Dayang Chem Co. (Hangzhou, China). Fluorescein isothiocyanate (FITC) was purchased from Sigma-Aldrich (St. Louis, MO, USA). Cyclovalone (https://pubchem.ncbi.nlm.nih.gov/compound/Cyclovalone) was kindly provided by Prof. Sergey S. Krylov (N.D. Zelinsky Institute of Organic Chemistry, Russian Academy of Sciences, Moscow, Russia). Therapeutic agents, including paclitaxel, doxorubicin, vincristine, cisplatin, glutathione (GSH), 4-methylumbelliferone (MUmb), curcumin, doxycycline, p-anisidine, 2-mercaptobenzimidazole, listed in Table 3, were obtained from commercial sources and dissolved in appropriate solvents. All other chemicals and solvents were of analytical grade and used without further purification.

3.2. Synthesis of Carbohydrate-Functionalized Fluorescent Ligands

A panel of five fluorescent ligands (L1–L5) was synthesized by conjugating specific carbohydrate moieties to a polyethyleneimine (PEI, 1.8 kDa) backbone labeled with fluorescein isothiocyanate (FITC), in accordance with our previously established protocols [37,73,74]. The synthesis proceeded via a sequential two-step strategy designed to optimize both fluorescence intensity and receptor recognition specificity.

First, the fluorescent precursor (PEI-FITC) was prepared by reacting PEI with FITC in anhydrous dimethyl sulfoxide (DMSO). The reaction was conducted in the dark at room temperature for 12 hours to achieve a PEI:FITC molar ratio of approximately 1:1, ensuring distinct labeling without compromising polymer solubility.

Subsequently, carbohydrate functionalization was performed using two distinct coupling chemistries selected based on the structural requirements of the target ligand.

Reductive Amination (Ligands L1, L3, L5). For linear mannose (ManLin, L1), linear galactose (GalLin, L3), and the branched trimannoside derivative (triMan-GlcNAc2, L5), conjugation was achieved via reductive amination. The specific carbohydrate was dissolved in borate buffer (pH 8.5) and added to the PEI-FITC solution. Sodium cyanoborohydride ($NaBH_3CN$) was added as a selective reducing agent. The mixture was stirred for 72 hours at room temperature, facilitating the formation of stable secondary amine linkages between the polymer amines and the open-chain aldehyde forms of the carbohydrates.

 doi:10.20944/preprints202603.1206.v1

CDI-Mediated Coupling (Ligands L2, L4). To synthesize ligands with cyclic carbohydrate presentation (ManCyc, L2 and GalCyc, L4), a 1,1′-carbonyldiimidazole (CDI)-mediated coupling reaction was employed to preserve the pyranose ring structure. The carbohydrate was pre-activated with CDI in anhydrous DMSO for 2 hours to generate the reactive imidazolyl carbamate intermediate. The PEI-FITC conjugate was then added, and the reaction proceeded for 24 hours. This method targets the primary hydroxyl groups of the sugars, forming stable carbamate linkages with the PEI backbone.

The molar ratios of reagents were strictly optimized for each ligand type (see Table 1) to achieve the desired degree of functionalization. The resulting polymer-based ligands were purified by extensive dialysis (MWCO 1000 Da) against deionized water for 48 hours to remove unreacted reagents, free carbohydrates, and salts, followed by lyophilization to obtain the final products as yellow-orange powders.

3.3. Instrumental Characterization of Carbohydrate-Functionalized Fluorescent Ligands

The chemical structure and purity of the synthesized conjugates were confirmed using spectroscopic methods. Fourier-transform infrared (FTIR) spectra of ligand solutions (10 mg/mL in PBS) were acquired using a Bruker Tensor 27 spectrometer (Bruker, Bremen, Germany) equipped with a liquid nitrogen-cooled mercury cadmium telluride (MCT) detector. Surface analysis of solid-state polymers was performed using a MICRAN-3 FTIR microscope (Simex, Novosibirsk, Russia), also utilizing a liquid nitrogen-cooled MCT detector.

Proton nuclear magnetic resonance (^{1}H NMR) spectra of the polymer solutions (20 mg/mL in D_2O) were recorded on a Bruker DRX-500 spectrometer operating at frequencies of 500.13 MHz for ^{1}H and 125.76 MHz for ^{13}C. Chemical shifts are reported in parts per million (ppm) and were referenced to the residual solvent signal.

The physicochemical properties of the ligands, including hydrodynamic diameter and surface charge (zeta-potential), were determined by dynamic light scattering (DLS) and electrophoretic light scattering, respectively. Measurements were conducted using a Zetasizer Nano S (Malvern Instruments, Worcestershire, UK) equipped with a 4 mW He–Ne laser (633 nm) at a fixed scattering angle of 173° and a temperature of 25 °C. Experimental data processing and analysis were performed using Zetasizer Software (v. 8.02).

The specific binding affinities of the synthesized ligands were assessed by determining the dissociation constant (K_{dis}) using a concanavalin A (ConA) binding assay, which serves as a validated model for mannose receptor interactions using a standardized protocol [74]. To evaluate ligand interactions, molecular dynamics (MD) simulations were performed for the CD206 receptor (PDB ID: 7JUE [75]). Simulations were conducted over 100 ns using NAMD with the AMBER ff14SB force field across three replicates [65]. Binding free energies were calculated utilizing the MM-PBSA method, which demonstrated a moderate correlation with experimental FTIR pK_d values ($r = 0.68$) . Furthermore, Concanavalin A (ConA) was validated as a robust structural model for CD206, exhibiting a high correlation ($r > 0.90$). To predict ligand affinities across all three target receptors—CD206, CD301 (PDB ID: 6PY1 [76]), and CD209 (PDB ID: 2IT5 [77])—we employed the Pafnucy neural network. This 3D convolutional neural network (3D-CNN), trained on the PDBbind2020 dataset, achieved an overall test accuracy of $r = 0.82$, and specifically $r = 0.80$ for CD206. Affinity predictions were generated utilizing voxel grid representations (20×20×20 Å, with a 0.5 Å resolution), and binding constants were derived via energy normalization according to the following equation $K_d = \exp((\Delta G+\alpha)/(R\cdot T))$.

3.4. Patient Samples and Ethical Statement

De-identified bronchoalveolar lavage fluid (BALF) samples were prospectively collected at the Clinical Hospital (Moscow, Russia) from ten pediatric patients (aged 6–16 years) presenting with diverse respiratory conditions, including bronchiectasis, bronchial asthma, and acute bronchitis. All

 doi:10.20944/preprints202603.1206.v1

procedures complied with the Declaration of Helsinki and were approved by the Local Ethics Committee (Protocol #2024-15A). Informed written consent was secured from the legal guardians of all participants prior to enrollment.

3.5. Isolation and In Vitro Remodeling of Alveolar Macrophages

Upon collection, BALF samples were immediately transported to the laboratory on ice to preserve cell viability. The fluid was filtered through a sterile 100-µm cell strainer to remove mucus and particulate debris. The cellular fraction was pelleted by centrifugation at 400 × g for 10 minutes at 4 °C. The supernatant was discarded, and the cell pellet was washed twice with cold sterile phosphate-buffered saline (PBS, pH 7.4).

The resulting cell pellet was resuspended in complete RPMI-1640 culture medium supplemented with 10% heat-inactivated fetal bovine serum (FBS), 2 mM L-glutamine, and a penicillin–streptomycin mixture (100 U/mL penicillin and 100 µg/mL streptomycin). BALF was analyzed both as a whole and after enrichment for the macrophage fraction.

Alveolar macrophages were enriched via adherence on mannan; the cell suspension was seeded into 96-well culture plates (coated with mannan) at a density of approximately 1×10^5 cells per well and incubated for 2 hours at 37 °C in a humidified 5% CO_2 atmosphere. Non-adherent cells (primarily lymphocytes and granulocytes) were removed by gentle washing with warm medium.

For the phenotypic remodeling assays, the adherent macrophage monolayers were incubated for 24 hours in fresh medium containing specific therapeutic agents (as listed in Table 3) at predetermined non-cytotoxic concentrations (100 µg/mL, and 30 µg/mL for doxorubicin and paclitaxel). Cells incubated in complete medium without additives served as the specific "intact" baseline control for each patient.

Flow cytometric analysis was conducted utilizing a BD FACSAria™ III Cell Sorter (BD Biosciences). To quantify the cellular uptake of the FITC-conjugated polymer, fluorescence intensity was measured using the FITC channel. The percentage of FITC-positive cells was subsequently recorded and compared across all experimental groups. Untreated cells, incubated in the absence of the polymer solution, were employed as a negative control to accurately establish baseline autofluorescence and define the gating parameters.

3.6. Fluorescent Fingerprint Analysis of BALF Samples – Macrophage Phenotyping

The experimental protocol commenced with isolation of cells from BALF, followed by plating the cell suspension into the wells of a microtiter plate to allow cellular adherence. Subsequently, a panel of fluorescent probes was introduced, and the mixture was incubated for 4 hours under controlled conditions. Fluorescence measurements were then performed on the reaction mixture, enabling calculation of binding parameters. Using five different fluorescent markers tested both in the presence and absence of mannans allowed generation of ten binding indices per sample, which constitute the basis for our fingerprint profiling approach.

The total reaction volume was maintained at 250 µL, containing approximately 1×10^6 BALF cells. The fluorescent marker was applied at final concentration of 0.05 mg/mL, while mannan as competitor was also used at 0.05 mg/mL. The assays were carried out in phosphate-buffered saline (PBS, 0.01 M, pH 7.4) at 37 °C for 4 h. Fluorescence of FITC-labeled markers was detected using a SpectraMax M5 microplate reader (Molecular Devices Corporation, California, USA) within black-walled Costar 96-well plates featuring clear bottoms. Excitation and emission wavelengths were set at 480 nm and 520 nm, respectively. The binding index, expressed as a percentage, was derived from the difference between initial and final fluorescence intensities, representing the proportion of fluorescent polymer bound to cells.

 doi:10.20944/preprints202603.1206.v1

3.7. Reference Macrophage Generation and Phenotypic Deconvolution Analysis

To establish quantitative reference signatures for phenotypic profiling, control macrophage populations were generated from peripheral blood mononuclear cells (PBMCs) obtained from healthy donors. PBMCs were isolated via density gradient centrifugation and differentiated into resting M0 macrophages by culturing in RPMI-1640 supplemented with 50 ng/mL macrophage colony-stimulating factor (M-CSF) for 7 days. Subsequently, M0 macrophages were polarized into the classically activated (M1) phenotype by incubation with 100 ng/mL lipopolysaccharide (LPS) and 20 ng/mL interferon-gamma (IFN-γ), or into the alternatively activated (M2a) phenotype using 20 ng/mL interleukin-4 (IL-4) for 24 hours.

The normalized ligand-binding fingerprints obtained from these phenotypically distinct reference populations (M0, M1, and M2a) served as the basis vector set. To determine the phenotypic composition of the patient samples, the multidimensional binding profiles of BALF macrophages were mathematically approximated as a linear combination of these three reference signatures. A constrained least squares minimization algorithm was employed to solve the system, minimizing the sum of squared residuals between the experimental BALF vector and the theoretical reconstructed vector [38]. This deconvolution approach allowed for the resolution of the complex BALF signal into the relative fractional contributions (%) of the M0, M1, and M2a subpopulations.

To assessing the therapeutic efficacy of the tested compounds, a Pearson correlation analysis was performed. The binding profile of each drug-treated sample was correlated against the averaged reference centroids derived from the "Good Prognosis" (Severity Score 0) and "Poor Prognosis" (Severity Score 5) clinical cohorts. A statistically significant positive shift in the correlation coefficient (r) toward the "Good Prognosis" reference profile was interpreted as a successful functional remodeling of the alveolar macrophages.

3.8. Computational Framework and Linear Discriminant Analysis (LDA)

To statistically discriminate between clinical prognostic groups based on complex macrophage ligand-binding signatures, a multivariate classification approach using Linear Discriminant Analysis (LDA) was employed. All computational procedures were executed within the Jupyter Lab interactive environment using the Python programming language (version 3.9). The analytical workflow integrated Pandas and NumPy libraries for data structuring, normalization, and pre-processing, while the Scikit-learn library was utilized for the implementation of the LDA algorithm. High-dimensional data visualization and canonical discriminant plotting were performed using Matplotlib and Seaborn.

The input feature matrix was constructed using ten quantitative variables per patient sample: the normalized binding indices of the five fluorescent ligands (L1–L5) measured under standard conditions, and the corresponding indices measured in the presence of competitive mannan (ML1–ML5). The clinical prognosis category ("Good", "Neutral", "Poor") served as the target variable.

The LDA algorithm projected the high-dimensional feature space onto a reduced canonical space (LD1 and LD2) optimized to maximize the ratio of between-class variance to within-class variance (Fisher's criterion). The first canonical discriminant function (LD1) was extracted to quantify the separation between favorable and unfavorable clinical outcomes. Model performance was evaluated using confusion matrices and classification accuracy scores calculated within the computational framework. Decision boundaries were visualized by generating a prediction mesh grid across the 2D canonical space to map the classification regions for each coordinate point.

3.9. Statistical Analysis

Quantitative data are presented as mean ± standard deviation (SD). Comparative analysis between "Good" and "Poor" prognostic profile groups was conducted using independent two-tailed Student's *t*-tests. A *p*-value of less than 0.05 was considered statistically significant. All statistical

 doi:10.20944/preprints202603.1206.v1

calculations were performed using the Python scipy.stats module and Origin 2024b statistical software.

4. Conclusions

The transition from empirical immunopharmacology to data-driven precision immune engineering requires a fundamental reassessment of how therapeutic interventions are evaluated. To address this challenge, we developed an ex vivo multiparametric test system specifically designed to detect secondary, off-target immunomodulatory effects of pharmacological agents on macrophages. By utilizing patient-derived bronchoalveolar lavage (BAL) samples to interrogate alveolar macrophage plasticity via carbohydrate-functionalized fluorescent ligands, the platform generates a highly sensitive, quantitative functional readout of the local immune microenvironment.

Unlike traditional frameworks that restrict macrophages to discrete phenotypic categories, our platform evaluates them across a continuous dynamic spectrum, encompassing pro-inflammatory, anti-inflammatory, and intermediate states. Processing the resulting high-dimensional ligand-binding fingerprints inherently requires artificial intelligence (AI) and machine learning (ML) frameworks. Algorithms such as neural networks and Random Forest are highly applicable for such multidimensional data, offering the capacity to identify complex non-linear patterns, predict disease severity prior to clinical manifestation, and stratify patients into distinct prognostic tiers.

Despite the broad utility of deep learning, we employed Linear Discriminant Analysis (LDA) for the integration of ligand-binding profiles in this study, as it provided a highly efficient, pragmatic, and computationally lightweight solution. LDA achieved an optimal balance between predictive accuracy and data transparency. It enabled the construction of distinct, quantitative immune-state vectors that reliably differentiate favorable prognostic signatures from imbalanced immune states, entirely avoiding the computational overhead and interpretive opacity characteristic of deep neural networks.

In translational terms, quantifying the terminal functional phenotype of macrophages proves more clinically actionable than tracking discrete intracellular drug signaling pathways. LDA modeling allowed us to quantitatively measure the phenotypic shifts of primary patient macrophages toward pro-inflammatory (M1), reparative (M2a), or dedifferentiated (M0) states. Consequently, the assay successfully captured the strong M2a-polarizing action of doxycycline, the pronounced M1-driving effect of 4-methylumbelliferone, and the profound M0-like dedifferentiation induced by paclitaxel.

The clinical validity of these induced phenotypes is strictly governed by the patient's baseline immune context. Our data confirm that while doxycycline's robust M2a polarization supports the resolution of acute neutrophilic inflammation, it represents a strict contraindication in Th2-driven diseases such as asthma, where excessive alternative activation exacerbates airway remodeling and fibrosis. The platform also demonstrated the efficacy of targeted natural adjuvants in correcting these adverse secondary pharmacological effects.

Functioning as a comprehensive immune sensitivity assay, the multiparametric test system, integrated with targeted machine learning algorithms, establishes a functional framework for personalized companion diagnostics. By centering on the quantitative measurement of terminal macrophage phenotypes, this approach advances the clinical management of severe respiratory pathologies from empirical, trial-and-error treatments to predictive, data-driven immune reconstruction.

Supplementary Materials: The following supporting information can be downloaded at: https://www.mdpi.com/article/doi/s1, **Figure S1.** A schematic representation of the synthesis of FITC-labeled fluorescence markers incorporating five different types of carbohydrates that have specific affinities for macrophage receptors, designed to detect them. **Figure S2.** FTIR spectra of FITC ligands with different affinity to CD206, CD301 macrophage receptors X-PEI-FITC. Conditions: PBS (0.01 M, pH 7.4); T = 37 °C. **Figure S3.** ^{1}H

 doi:10.20944/preprints202603.1206.v1

NMR spectra of (a) triMan-GlcNAc2, (b) PEI1.8-triMan with proton assignment. D_2O, 400 MHz. **Figure S4.** Flow cytometry results of macrophages incubated with X-PEI-FITC polymer samples. Concentration of polymers is 0.1 mg/mL. Data are presented by overlaid histograms of control macrophages (blue) and macrophages after incubation with sample (red) represented by histograms. **Figure S5.** Feature importance for linear discriminant analysis. Bar chart ranking the top 20 features contributing to the LD1 discriminant function. **Figure S6.** Mannan-mediated inhibition of ligand binding**.** Scatter plots comparing ligand binding in the absence (x-axis) versus presence (y-axis) of mannan inhibition. The diagonal dashed line represents zero inhibition (non-specific binding). 'Good' prognosis samples (green) typically show distinct inhibition patterns (deviation from diagonal), whereas 'Poor' prognosis samples (red) often exhibit aberrant binding behaviors, reflecting the loss of functional receptor specificity identified by the LDA model. **Table S1.** LDA-derived contributions of canonical macrophage states in intact and drug-treated BAL samples from pediatric patients. For each patient (P1–P10) and each ex vivo condition (intact BAL and the indicated compounds), the relative contributions (%) of the reference M0-, M1- and M2a-like signatures, together with the residual fraction not captured by these three archetypes, are listed. **Table S2.** Systematic analysis of pharmacological modulators of macrophage polarization: mechanisms and pulmonary applications. .

Author Contributions: Conceptualization, E.V.K., I.D.Z.; methodology, I.D.Z. V.A.A. and E.V.K.; formal analysis, I.D.Z.; investigation, I.D.Z., V.A.A. and E.V.K.; data curation, I.D.Z.; writing—original draft preparation, I.D.Z.; writing—review and editing, E.V.K.; project supervision, E.V.K.; funding acquisition, E.V.K. All authors have read and agreed to the published version of the manuscript.

Institutional Review Board Statement: Cell lines were obtained from Lomonosov Moscow State University Depository of Live Systems Collection (Moscow, Russia).

Informed Consent Statement: BALF samples were obtained from Clinical Hospital following patient consent and strict adherence to ethical guidelines (approved by the Local Ethics Committee, Protocol #2024-15A).

Data Availability Statement: The data presented in this study are available in the main text and in Supplementary Materials.

Conflicts of Interest: The authors declare no conflicts of interest.

Abbreviations

The following abbreviations are used in this manuscript:

BAL	Bronchoalveolar lavage
BALF	Bronchoalveolar lavage fluid
CLSM	Confocal laser scanning microscopy
CPR	C-reactive protein
DAPI	4',6-diamidino-2-phenylindole
DOPS	Dioleoyl phosphatidylserine
FTIR	Fourier-transformed infrared spectroscopy

References

1. Brancewicz, J.; Wójcik, N.; Sarnowska, Z.; Robak, J.; Król, M. The Multifaceted Role of Macrophages in Biology and Diseases. *Int. J. Mol. Sci.* **2025**, *26*, 1–26, doi:10.3390/ijms26052107.
2. Yuan, R.; Ma, Y.; Yang, C.; Li, L. Plasticity of Monocytes/Macrophages: Phenotypic Changes during Disease Progression. *Front. Immunol.* **2023**, *14*, 1–2, doi:10.3389/fimmu.2023.1328382.
3. Stout, R.D.; Suttles, J. Immunosenescence and Macrophage Functional Plasticity: Dysregulation of Macrophage Function by Age-Associated Microenvironmental Changes. *Immunol. Rev.* **2005**, *205*, 60–71, doi:10.1111/j.0105-2896.2005.00260.x.
4. Mowat, A.M.I.; Scott, C.L.; Bain, C.C. Barrier-Tissue Macrophages: Functional Adaptation to Environmental Challenges. *Nat. Med.* **2017**, *23*, 1258–1270, doi:10.1038/nm.4430.

 doi:10.20944/preprints202603.1206.v1

5. Galli, S.J.; Borregaard, N.; Wynn, T.A. Phenotypic and Functional Plasticity of Cells of Innate Immunity: Macrophages, Mast Cells and Neutrophils. *Nat. Immunol.* **2011**, *12*, 1035–1044, doi:10.1038/ni.2109.
6. Stout, R.D.; Suttles, J. Functional Plasticity of Macrophages: Reversible Adaptation to Changing Microenvironments. *J. Leukoc. Biol.* **2004**, *76*, 509–513, doi:10.1189/jlb.0504272.
7. Libby, P.; Smith, R.; Rubin, E.J.; Glassberg, M.K.; Farkouh, M.E.; Rosenson, R.S. Inflammation Unites Diverse Acute and Chronic Diseases. *Eur. J. Clin. Invest.* **2024**, *54*, 1–12, doi:10.1111/eci.14280.
8. Porta, C.; Riboldi, E.; Totaro, M.G.; Strauss, L.; Sica, A.; Mantovani, A. Macrophages in Cancer and Infectious Diseases: The "good" and the "Bad." *Immunotherapy* **2011**, *3*, 1185–1202, doi:10.2217/imt.11.116.
9. Sarbayeva, N.N.; Ponomareva, Yu.V.; Milyakova M.N. Macrophages: Diversity Of Phenotypes And Functions, Interaction With Foreign Materials. Genes And Cells **2016**, *11*, 9–17.
10. Brundu S, F.A. Polarization and Repolarization of Macrophages. *J. Clin. Cell. Immunol.* **2015**, *06*, doi:10.4172/2155-9899.1000319.
11. Ge, Z.; Chen, Y.; Ma, L.; Hu, F.; Xie, L. Macrophage Polarization and Its Impact on Idiopathic Pulmonary Fibrosis. *Front. Immunol.* **2024**, *15*, doi:10.3389/fimmu.2024.1444964.
12. Nandakumar, V.; Hebrink, D.; Jenson, P.; Kottom, T.; Limper, A.H. Differential Macrophage Polarization from Pneumocystis in Immunocompetent and Immunosuppressed Hosts: Potential Adjunctive Therapy during Pneumonia. *Infect. Immun.* **2017**, *85*, doi:10.1128/IAI.00939-16.
13. Hong, J.Y.; Chung, Y.; Steenrod, J.; Chen, Q.; Lei, J.; Comstock, A.T.; Goldsmith, A.M.; Bentley, J.K.; Sajjan, U.S.; Hershenson, M.B. Macrophage Activation State Determines the Response to Rhinovirus Infection in a Mouse Model of Allergic Asthma. *Respir. Res.* **2014**, *15*, 1–15, doi:10.1186/1465-9921-15-63.
14. Peng, G.; Duan, T.; Guo, M.; Xue, Y.; Chen, C.; Li, Y.; Leifer, K.; Fadeel, B. Biodegradation of Graphdiyne Oxide in Classically Activated (M1) Macrophages Modulates Cytokine Production. *Nanoscale* **2021**, *13*, 13072–13084, doi:10.1039/d1nr02473f.
15. Peng, Y.; Zhou, M.; Yang, H.; Qu, R.; Qiu, Y.; Hao, J.; Bi, H.; Guo, D. Regulatory Mechanism of M1/M2 Macrophage Polarization in the Development of Autoimmune Diseases. *Mediators Inflamm.* **2023**, *2023*, 1–20, doi:10.1155/2023/8821610.
16. Cutolo, M.; Campitiello, R.; Gotelli, E.; Soldano, S. The Role of M1/M2 Macrophage Polarization in Rheumatoid Arthritis Synovitis. *Front. Immunol.* **2022**, *13*, 1–14, doi:10.3389/fimmu.2022.867260.
17. Arabpour, M.; Saghazadeh, A.; Rezaei, N. Anti-Inflammatory and M2 Macrophage Polarization-Promoting Effect of Mesenchymal Stem Cell-Derived Exosomes. *Int. Immunopharmacol.* **2021**, *97*, 107823, doi:10.1016/j.intimp.2021.107823.
18. Weinhäuser, I.; Pereira-Martins, D.A.; Almeida, L.Y.; Hilberink, J.R.; Silveira, D.R.A.; Quek, L.; Ortiz, C.; Araujo, C.L.; Bianco, T.M.; Lucena-Araujo, A.; et al. M2 Macrophages Drive Leukemic Transformation by Imposing Resistance to Phagocytosis and Improving Mitochondrial Metabolism. *Sci. Adv.* **2023**, *9*, 1–21, doi:10.1126/sciadv.adf8522.
19. Wang, Y.; Lin, Q.; Zhang, H.; Wang, S.; Cui, J.; Hu, Y.; Liu, J.; Li, M.; Zhang, K.; Zhou, F.; et al. M2 Macrophage-Derived Exosomes Promote Diabetic Fracture Healing by Acting as an Immunomodulator. *Bioact. Mater.* **2023**, *28*, 273–283, doi:10.1016/j.bioactmat.2023.05.018.
20. Mills, C.D. Anatomy of a Discovery: M1 and M2 Macrophages. *Front. Immunol.* **2015**, *6*, 1–12, doi:10.3389/fimmu.2015.00212.
21. Italiani, P.; Boraschi, D. From Monocytes to M1/M2 Macrophages: Phenotypical vs. Functional Differentiation. *Front. Immunol.* **2014**, *5*, 1–22, doi:10.3389/fimmu.2014.00514.
22. Toews, G.B. *Macrophages*; Rousselet, G., Ed.; Methods in Molecular Biology; Springer New York: New York, NY, 2008; Vol. 1784; ISBN 9780123740014.
23. Lepekha, L.N.; Erokhina, M.V.; Demyanenko, N.G.; Shcherbakova, E.A.; Ergeshov, A.E. Macrophage Phenotypic Plasticity during Inflammation in Patients with Pulmonary Sarcoidosis or Tuberculosis. *Вестник Цниит* **2022**, 7–21, doi:10.57014/2587-6678-2022-3-7-21.
24. Qiaozhen, H.; Jifei, Z.; Lingrong, H.; Qiuming, Y.; Hongjuan, Y.; Qiaozhen, H. Clinical Significance of Detection of Mononuclear Phagocyte Subsets in Blood and Bronchoalveolar Lavage Fluid (BALF) in Pulmonary Sarcoidosis. *Cell. Mol. Biol.* **2021**, *67*, 109–116, doi:10.14715/CMB/2021.67.5.15.

25. Sun, K.; Dong, J.; Mao, X.; Li, W.; Wang, Y.; Teng, X.; Liu, D.; Yang, B. CD160 + Intraepithelial Lymphocytes and CCRL2 + Macrophages Drive Differential Repair in Cardiac and Liver Injuries. *Cell. Mol. Immunol.* **2025**, doi:10.1038/s41423-025-01376-6.
26. Biswas, S.K.; Chittezhath, M.; Shalova, I.N.; Lim, J.-Y. Macrophage Polarization and Plasticity in Health and Disease. *Immunol. Res.* **2012**, *53*, 11–24, doi:10.1007/s12026-012-8291-9.
27. Fiani, M.L.; Barreca, V.; Sargiacomo, M.; Ferrantelli, F.; Manfredi, F.; Federico, M. Exploiting Manipulated Small Extracellular Vesicles to Subvert Immunosuppression at the Tumor Microenvironment through Mannose Receptor/CD206 Targeting. *Int. J. Mol. Sci.* **2020**, *21*, 1–20, doi:10.3390/ijms21176318.
28. Cassetta, L.; Pollard, J.W. Repolarizing Macrophages Improves Breast Cancer Therapy. *Cell Res.* **2017**, *27*, 963–964, doi:10.1038/cr.2017.63.
29. Alizadeh, D.; Zhang, L.; Hwang, J.; Schluep, T.; Badie, B. Tumor-Associated Macrophages Are Predominant Carriers of Cyclodextrin-Based Nanoparticles into Gliomas. *Nanomedicine* **2010**, *6*, 382–390, doi:10.1016/j.nano.2009.10.001.
30. An, Y.; Yang, Q. Tumor-Associated Macrophage-Targeted Therapeutics in Ovarian Cancer. *Int. J. Cancer* **2021**, *149*, 21–30, doi:10.1002/ijc.33408.
31. Barrow, E.L.W.; Winchester, G.A.; Staas, J.K.; Quenelle, D.C.; Barrow, W.W. Use of Microsphere Technology for Targeted Delivery of Rifampin to Mycobacterium Tuberculosis-Infected Macrophages. *Antimicrob. Agents Chemother.* **1998**, *42*, 2682–2689, doi:10.1128/aac.42.10.2682.
32. Dua, K.; Rapalli, V.K.; Shukla, S.D.; Singhvi, G.; Shastri, M.D.; Chellappan, D.K.; Satija, S.; Mehta, M.; Gulati, M.; Pinto, T.D.J.A.; et al. Multi-Drug Resistant Mycobacterium Tuberculosis & Oxidative Stress Complexity: Emerging Need for Novel Drug Delivery Approaches. *Biomedicine and Pharmacotherapy* **2018**, *107*, 1218–1229, doi:10.1016/j.biopha.2018.08.101.
33. Mills, C.D. Anatomy of a Discovery: M1 and M2 Macrophages. *Front. Immunol.* **2015**, *6*, 1–12, doi:10.3389/fimmu.2015.00212.
34. Kwon, D.H.; Lee, H.; Park, C.; Hong, S.H.; Hong, S.H.; Kim, G.Y.; Cha, H.J.; Kim, S.; Kim, H.S.; Hwang, H.J.; et al. Glutathione Induced Immune-Stimulatory Activity by Promoting M1-like Macrophages Polarization via Potential ROS Scavenging Capacity. *Antioxidants* **2019**, *8*, 1–18, doi:10.3390/antiox8090413.
35. Kim, G.-D.; Lim, E.Y.; Shin, H.S. Macrophage Polarization and Functions in Pathogenesis of Chronic Obstructive Pulmonary Disease. *Int. J. Mol. Sci.* **2024**, *25*, 5631, doi:10.3390/ijms25115631.
36. Lee, J.; Arisi, I.; Puxeddu, E.; Mramba, L.K.; Amicosante, M.; Swaisgood, C.M.; Pallante, M.; Brantly, M.L.; Sköld, C.M.; Saltini, C. Bronchoalveolar Lavage (BAL) Cells in Idiopathic Pulmonary Fibrosis Express a Complex pro-Inflammatory, pro-Repair, Angiogenic Activation Pattern, Likely Associated with Macrophage Iron Accumulation. *PLoS One* **2018**, *13*, e0194803, doi:10.1371/journal.pone.0194803.
37. Zlotnikov, I.D.; Kudryashova, E. V. Polymeric Infrared and Fluorescent Probes to Assess Macrophage Diversity in Bronchoalveolar Lavage Fluid of Asthma and Other Pulmonary Disease Patients. *Polymers (Basel).* **2024**, *16*, 3427, doi:10.3390/polym16233427.
38. Zlotnikov, I.D.; Ezhov, A.A.; Kudryashova, E. V. A Glycan-Based Ligands for Phenotypic Profiling and Selective Immunomodulation of Alveolar Macrophage for Resolution of Inflammation. *Immuno* **2026**, *6*, doi:10.3390/immuno6010009.
39. Zlotnikov, I.D.; Kolganova, N.I.; Gitinov, S.A.; Ovsyannikov, D.Y.; Kudryashova, E. V. The Role of CD68+ Cells in Bronchoalveolar Lavage Fluid for the Diagnosis of Respiratory Diseases. *Immuno* **2025**, *5*, doi:10.3390/immuno5030043.
40. Wen, L.; Lyu, L.; Wu, W.; Wang, Y.; Ding, B.; Dai, Z. Gpx1 Induces M2 Polarization of Macrophages, Contributing to Doxorubicin Resistance in Triple-Negative Breast Cancer. *Hum. Immunol.* **2025**, *86*, 111566, doi:10.1016/j.humimm.2025.111566.
41. Degboé, Y.; Poupot, R.; Poupot, M. Repolarization of Unbalanced Macrophages: Unmet Medical Need in Chronic Inflammation and Cancer. *Int. J. Mol. Sci.* **2022**, *23*, 1496, doi:10.3390/ijms23031496.
42. Wang, P.; Wang, H.; Huang, Q.; Peng, C.; Yao, L.; Chen, H.; Qiu, Z.; Wu, Y.; Wang, L.; Chen, W. Exosomes from M1-Polarized Macrophages Enhance Paclitaxel Antitumor Activity by Activating Macrophages-Mediated Inflammation. *Theranostics* **2019**, *9*, 1714–1727, doi:10.7150/thno.30716.

 doi:10.20944/preprints202603.1206.v1

43. Gao, S.; Zhou, J.; Liu, N.; Wang, L.; Gao, Q.; Wu, Y.; Zhao, Q.; Liu, P.; Wang, S.; Liu, Y.; et al. Curcumin Induces M2 Macrophage Polarization by Secretion IL-4 and/or IL-13. *J. Mol. Cell. Cardiol.* **2015**, *85*, 131–139, doi:10.1016/j.yjmcc.2015.04.025.
44. Zhou, Y.; Zhang, T.; Wang, X.; Wei, X.; Chen, Y.; Guo, L.; Zhang, J.; Wang, C. Curcumin Modulates Macrophage Polarization Through the Inhibition of the Toll-Like Receptor 4 Expression and Its Signaling Pathways. *Cellular Physiology and Biochemistry* **2015**, *36*, 631–641, doi:10.1159/000430126.
45. Lu, X.; Zhang, P.; Li, J.; Zhou, Y.; Wang, B.; Lu, Z. The Effect of Doxorubicin Curcumin Co − Loaded Lipid Nanoparticles and Doxorubicin on Osteosarcoma before Surgery. *Cancer Nanotechnol.* **2024**, 1–11, doi:10.1186/s12645-024-00247-5.
46. Ashrafizadeh, M.; Zarrabi, A.; Hashemi, F.; Zabolian, A.; Hushmandi, K.; Ang, H.L.; Makvandi, P.; Khan, H. *Polychemotherapy with Curcumin and Doxorubicin* via *Biological Nanoplatforms : Enhancing Antitumor Activity*; 2020; ISBN 1916893813.
47. Mishra, S.; Pandey, A.; Manvati, S. Coumarin: An Emerging Antiviral Agent. *Heliyon* **2020**, *6*, e03217, doi:10.1016/j.heliyon.2020.e03217.
48. Gupta, D.; Guliani, E.; Bajaj, K. Coumarin—Synthetic Methodologies, Pharmacology, and Application as Natural Fluorophore. *Top. Curr. Chem.* 2024, *382*.
49. He, L.; Marneros, A.G. Doxycycline Inhibits Polarization of Macrophages to the Proangiogenic M2-Type and Subsequent Neovascularization. *Journal of Biological Chemistry* **2014**, *289*, 8019–8028, doi:10.1074/jbc.M113.535765.
50. Cortés, M.; Brischetto, A.; Martinez-Campanario, M.C.; Ninfali, C.; Domínguez, V.; Fernández, S.; Celis, R.; Esteve-Codina, A.; Lozano, J.J.; Sidorova, J.; et al. Inflammatory Macrophages Reprogram to Immunosuppression by Reducing Mitochondrial Translation. *Nat. Commun.* **2023**, *14*, doi:10.1038/s41467-023-42277-4.
51. Zlotnikov, I.D.; Krylov, S.S.; Belogurova, N.G.; Blinnikov, A.N.; Kalugin, V.E.; Kudryashova, E. V. New Derivatives of Chalcones, Chromenes, and Stilbenoids, Complexed with Methyl-β-Cyclodextrin with Antioxidant Properties and Antibacterial Synergism with Antibiotics. *Biophysica* **2024**, *4*, 667–694, doi:10.3390/biophysica4040044.
52. Varakutin, A.E.; Muravsky, E.A.; Tsyganov, D. V.; Shinkarev, I.Y.; Samigullina, A.I.; Kuptsova, T.S.; Chuprov-Netochin, R.N.; Smirnova, A. V.; Khomutov, A.A.; Leonov, S. V.; et al. Synthesis of Chalcones with Methylenedioxypolymethoxy Fragments Based on Plant Metabolites and Study of Their Antiproliferative Properties. *Russian Chemical Bulletin* **2023**, *72*, 1632–1647, doi:10.1007/s11172-023-3943-6.
53. d'Alessandro, M.; Carleo, A.; Cameli, P.; Bergantini, L.; Perrone, A.; Vietri, L.; Lanzarone, N.; Vagaggini, C.; Sestini, P.; Bargagli, E. BAL Biomarkers' Panel for Differential Diagnosis of Interstitial Lung Diseases. *Clin. Exp. Med.* **2020**, *20*, 207–216, doi:10.1007/s10238-020-00608-5.
54. Todd, J.L.; Weber, J.M.; Kelly, F.L.; Neely, M.L.; Mulder, H.; Frankel, C.W.; Nagler, A.; McCrae, C.; Newbold, P.; Kreindler, J.; et al. BAL Fluid Eosinophilia Associates With Chronic Lung Allograft Dysfunction Risk: A Multicenter Study. *Chest* **2023**, *164*, 670–681, doi:10.1016/j.chest.2023.03.033.
55. Gao, C.A.; Cuttica, M.J.; Malsin, E.S.; Argento, A.C.; Wunderink, R.G.; Smith, S.B. Comparing Nasopharyngeal and BAL SARS-CoV-2 Assays in Respiratory Failure. *Am. J. Respir. Crit. Care Med.* **2021**, *203*, 127–129, doi:10.1164/rccm.202008-3137LE.
56. Rai, R.K.; Azim, A.; Sinha, N.; Sahoo, J.N.; Singh, C.; Ahmed, A.; Saigal, S.; Baronia, A.K.; Gupta, D.; Gurjar, M.; et al. Metabolic Profiling in Human Lung Injuries by High-Resolution Nuclear Magnetic Resonance Spectroscopy of Bronchoalveolar Lavage Fluid (BALF). *Metabolomics* **2013**, *9*, 667–676, doi:10.1007/s11306-012-0472-y.
57. Van Rijt, L.S.; Kuipers, H.; Vos, N.; Hijdra, D.; Hoogsteden, H.C.; Lambrecht, B.N. A Rapid Flow Cytometric Method for Determining the Cellular Composition of Bronchoalveolar Lavage Fluid Cells in Mouse Models of Asthma. *J. Immunol. Methods* **2004**, *288*, 111–121, doi:10.1016/j.jim.2004.03.004.
58. Drent, M.; Jacobs, J.A. Bronchoalveolar Lavage. *Encyclopedia of Respiratory Medicine: Volume 1-4* **2006**, *1–4*, V1-275-V1-284, doi:10.1016/B0-12-370879-6/00051-X.

 doi:10.20944/preprints202603.1206.v1

59. St-Laurent, J.; Turmel, V.; Boulet, L.P.; Bissonnette, E. Alveolar Macrophage Subpopulations in Bronchoalveolar Lavage and Induced Sputum of Asthmatic and Control Subjects. *Journal of Asthma* **2009**, *46*, 1–8, doi:10.1080/02770900802444211.
60. Rose, A.S.; Knox, K.S. Bronchoalveolar Lavage as a Research Tool. *Semin. Respir. Crit. Care Med.* **2007**, *28*, 561–573, doi:10.1055/s-2007-991528.
61. Davidson, K.R.; Ha, D.M.; Schwarz, M.I.; Chan, E.D. Bronchoalveolar Lavage as a Diagnostic Procedure: A Review of Known Cellular and Molecular Findings in Various Lung Diseases. *J. Thorac. Dis.* **2020**, *12*, 4991–5019, doi:10.21037/jtd-20-651.
62. Zlotnikov, I.D.; Ezhov, A.A.; Kolganova, N.I.; Ovsyannikov, D.Y.; Belogurova, N.G.; Kudryashova, E. V. Optical Methods for Determining the Phagocytic Activity Profile of CD206-Positive Macrophages Extracted from Bronchoalveolar Lavage by Specific Mannosylated Polymeric Ligands. *Polymers (Basel).* **2025**, *17*, doi:10.3390/polym17010065.
63. Oates, T.; Moura, P.; Cross, S.; Roberts, K.; Baum, H.; Haydn-Smith, K.; Wilson, M.; Heesom, K.; Severn, C.; Toye, A. Characterizing the Polarization Continuum of Macrophage Subtypes M1, M2a and M2c 2022.
64. Zlotnikov, I.D.; Kudryashova, E. V. Biomimetic System Based on Reconstituted Macrophage Membranes for Analyzing and Selection of Higher-Affinity Ligands Specific to Mannose Receptor to Develop the Macrophage-Focused Medicines. *Biomedicines* **2023**, *11*, doi:10.3390/biomedicines11102769.
65. Zlotnikov, I.D.; Kudryashova, E. V. Computer Simulation of the Receptor–Ligand Interactions of Mannose Receptor CD206 in Comparison with the Lectin Concanavalin A Model. *Biochemistry (Moscow)* **2022**, *87*, 54–69, doi:10.1134/S0006297922010059.
66. Stepniewska-Dziubinska, M.M.; Zielenkiewicz, P.; Siedlecki, P. Development and Evaluation of a Deep Learning Model for Protein–Ligand Binding Affinity Prediction. *Bioinformatics* **2018**, *34*, 3666–3674, doi:10.1093/bioinformatics/bty374.
67. Sharma, M.; Khaitan, T.; Raman, S.; Jain, R. Determination of Serum IgE and Eosinophils as a Diagnostic Indicator in Allergic Rhinitis. *Indian Journal of Otolaryngology and Head & Neck Surgery* **2018**, doi:10.1007/s12070-018-1383-7.
68. Grwnberger, P.A.; Smith, L.J.; Hsu, C.C.S.; Roberts, M.; Liotta, J.L.; Chicago, B.S. Analysis of Bronchoalveolar Lavage in Allergic Bronchopulmonary Aspergillosis: Divergent Responses of Antigen-Specific Antibodies and Total IgE;
69. Yun, Y.; Kanda, A.; Kobayashi, Y.; Van Bui, D.; Suzuki, K.; Sawada, S.; Baba, K.; Yagi, M.; Asako, M.; Okazaki, H.; et al. Increased CD69 Expression on Activated Eosinophils in Eosinophilic Chronic Rhinosinusitis Correlates with Clinical Findings. *Allergology International* **2020**, *69*, 232–238, doi:10.1016/j.alit.2019.11.002.
70. Kostikas, K.; Brindicci, C.; Patalano, F. Blood Eosinophils as Biomarkers to Drive Treatment Choices in Asthma and COPD. *Curr. Drug Targets* **2018**, *19*, 1882–1896, doi:10.2174/1389450119666180212120012.
71. Tacconi, S.; Jalabert, A.; Berger, E.; Cotte, C.; Errazuriz-cerda, E.; Bardot, V.; Leblanc, A.; Berthomier, L.; Dubourdeaux, M.; Rome, S. Microvesicles from Turmeric Extracts Contain Curcuminoids and Modulate Macrophage Polarization and Migration. **2025**, 1–13.
72. Zlotnikov, I.D.; Belogurova, N.G.; Krylov, S.S.; Semenova, M.N.; Semenov, V. V.; Kudryashova, E. V. Plant Alkylbenzenes and Terpenoids in the Form of Cyclodextrin Inclusion Complexes as Antibacterial Agents and Levofloxacin Synergists. *Pharmaceuticals* **2022**, *15*, doi:10.3390/ph15070861.
73. Zlotnikov, I.D.; Ezhov, A.A.; Petrov, R.A.; Vigovskiy, M.A.; Grigorieva, O.A.; Belogurova, N.G.; Kudryashova, E. V. Mannosylated Polymeric Ligands for Targeted Delivery of Antibacterials and Their Adjuvants to Macrophages for the Enhancement of the Drug Efficiency. *Pharmaceuticals* **2022**, *15*, 1172, doi:10.3390/ph15101172.
74. Zlotnikov, I.D.; Vigovskiy, M.A.; Davydova, M.P.; Danilov, M.R.; Dyachkova, U.D.; Grigorieva, O.A.; Kudryashova, E. V. Mannosylated Systems for Targeted Delivery of Antibacterial Drugs to Activated Macrophages. *Int. J. Mol. Sci.* **2022**, *23*, 1–29, doi:10.3390/ijms232416144.
75. Feinberg, H.; Jégouzo, S.A.F.; Lasanajak, Y.; Smith, D.F.; Drickamer, K.; Weis, W.I.; Taylor, M.E. Structural Analysis of Carbohydrate Binding by the Macrophage Mannose Receptor CD206. *Journal of Biological Chemistry* **2021**, *296*, 100368, doi:10.1016/j.jbc.2021.100368.

 doi:10.20944/preprints202603.1206.v1

76. Gabba, A.; Bogucka, A.; Luz, J.G.; Diniz, A.; Coelho, H.; Corzana, F.; Cañada, F.J.; Marcelo, F.; Murphy, P. V.; Birrane, G. Crystal Structure of the Carbohydrate Recognition Domain of the Human Macrophage Galactose C-Type Lectin Bound to GalNAc and the Tumor-Associated Tn Antigen. *Biochemistry* **2021**, *60*, 1327–1336, doi:10.1021/acs.biochem.1c00009.
77. Feinberg, H.; Castelli, R.; Drickamer, K.; Seeberger, P.H.; Weis, W.I. Multiple Modes of Binding Enhance the Affinity of DC-SIGN for High Mannose N-Linked Glycans Found on Viral Glycoproteins. *Journal of Biological Chemistry* **2007**, *282*, 4202–4209, doi:10.1074/jbc.M609689200.